Exhumation of deep continental crust in a transpressive regime: The example of Variscan eclogites from the Aiguilles-Rouges massif (Western Alps)

Jonas Vanardois, Françoise Roger, Pierre Trap, Philippe Goncalves, Pierre Lanari, Jean-louis Paquette, Didier Marquer, Florence Cagnard, Benjamin Le Bayon, Jérémie Melleton, et al.

Vanardois Jonas (Orcid ID: 0000-0003-3565-8219)

ROGER Françoise (Orcid ID: 0000-0003-3621-0213)

Goncalves Philippe (Orcid ID: 0000-0001-8069-7976)

Lanari Pierre (Orcid ID: 0000-0001-8303-0771)

Exhumation of deep continental crust in a transpressive regime: the example of Variscan eclogites from the Aiguilles-Rouges Massif (Western Alps).

Jonas Vanardois[1]*, Françoise Roger[2], Pierre Trap[1], Philippe Goncalves[1], Pierre Lanari[3], Jean-Louis Paquette[4], Didier Marquer[1], Florence Cagnard[5], Benjamin Le Bayon[5], Jérémie Melleton[5] and Fabrice Barou[2].

jonas.vanardois@univ-fcomte.fr; francoise.roger@umontpellier.fr; pierre.trap@univ-fcomte.fr; philippe.goncalves@univ-fcomte.fr; pierre.lanari@geo.unibe.ch; j.l.paquette@opgc.univ-bpclermont.fr; didier.marquer@univ-fcomte.fr; f.cagnard@brgm.fr; b.lebayon@brgm.fr; j.melleton@brgm.fr; fabrice.barou@umontpellier.fr.

[1]UMR 6249 Chrono-environnement, Université de Bourgogne-Franche-Comté, 25030 Besançon, France.

[2]Géosciences Montpellier, Campus Triolet, Université Montpellier, CNRS, 34095 Montpellier Cedex 5, France.

[3]Institute of Geological Sciences, University of Bern, Baltzerstrasse 3, Bern, CH-3012 Switzerland

This article has been accepted for publication and undergone full peer review but has not been through the copyediting, typesetting, pagination and proofreading process which may lead to differences between this version and the Version of Record. Please cite this article as doi: 10.1002/jmg.12659

[4]Laboratoire Magmas et Volcans (CNRS-UMR 6524), Campus Universitaire des Cézeaux, 63178 Aubière Cedex, France.

[5]BRGM-French Geological Survey, 3 Avenue Claude Guillemin, 45100, Orléans, France.

*Corresponding author: jonas.vanardois@univ-fcomte.fr +33(0)381666242 Present address: 16 route de Gray, 25030 Besançon.

Abstract:

Mafic eclogites are found in many orogens as lenses embedded in quartzo-feldspathic migmatites. These high-pressure relics are interpreted either as remnants of ancient sutures and thus formed during oceanic subduction, or as fragments of lower crust exhumed from the root of orogenic thickened crust. It is critical to distinguish between these two end-member scenarios as the resulting paleogeographic and geodynamic reconstructions may significantly differ. In this contribution, we investigated eclogite relics from Lac Cornu in the Aiguilles-Rouges massif, one of the External Crystalline Massifs of the Western Alps. Phase equilibrium modelling suggests that these mafic rocks were buried along a prograde path (M1) from ~600 °C/1.2–1.6 GPa to peak conditions of ~630–775 °C and >1.6 GPa. Zircon rims, with a rare earth element signature typical of eclogite facies zircon (no Eu anomalies, flat HREE spectrum), and rutile were dated by U-Th-Pb laser ablation-inductively coupled plasma-mass spectrometry (LA-ICPMS) at *c.* 335–330 Ma. Prograde deformation has not been identified in the field and is only recognized thanks to the crystallographic preferred orientation (CPO) of inclusions of omphacite and rutile in garnet. Peak pressure conditions were followed by a decompression stage (M2) from ~760 °C/1.4 GPa to ~600–650°C/0.9 GPa supported by the breakdown of omphacite into plagioclase-clinopyroxene symplectite and the crystallization of plagioclase-amphibole corona around garnet. The M2 retrogression stage is associated with the development of a main sub-horizontal planar fabric and the crystallographic preferred orientations of minerals composing symplectite. This deformation stage is interpreted as the result of horizontal lower-crustal flow. The final stage of exhumation (M3) is characterized by the replacement of symplectite and garnet by plagioclase and large euhedral amphibole and by the breakdown of rutile and ilmenite into titanite dated at *c.* 300 Ma. The crystallographic preferred orientations of titanite and amphibole are consistent with the development of vertical dextral shear zone in a transpressive regime. The combination of field observations, petrological, microtextural and geochemical analyses, suggests that the mafic eclogites preserved in migmatitic rocks of the Aiguilles-Rouges massif are remnants of a continental lower-crust exhumed and juxtaposed with lower-grade migmatites in crustal-scale vertical transpressive shear zones.

Keywords: External Crystalline Massif; Eclogite; Petrochronology; LA-ICPMS U-Th-Pb dating of zircon, rutile and titanite, EBSD

1. Introduction

Eclogites record fundamental processes related to high-pressure (HP) metamorphism associated with the burial and exhumation of crustal material. More generally eclogites give insight into the way crustal material flows during an orogenic event (e.g. Chopin, 1984; Spalla et al., 1996; Duchene et al., 1997; Lardeaux et al., 2001; O'Brien et al., 2001; Lanari et al., 2013). Eclogitic rocks have been identified in most of the massifs forming the hinterland of the Paleozoic Variscan belt (Fig. 1A), which is often considered as an analogue to the Tibetan-Himalayan orogenic plateau (e.g. Maierová et al., 2016). In these massifs, eclogites commonly occur as meter-scale lenses embedded in felsic migmatites preserving mineral assemblages equilibrated at lower pressure conditions (e.g. Štípská et al., 2006; Whitney et al., 2015, 2020; Ferrando et al., 2008; Jacob et al., 2021). In the Variscan belt, the eclogite relicts were often interpreted as remnants of suture zones (e.g. Lardeaux et al., 2001; Guillot & Ménot, 2009; Rubatto et al., 2010; Jouffray et al., 2020; Pitra et al., 2021). However, some of these eclogitic occurrences were also interpreted as the remants of thickened orogenic crust (e.g. Whitney et al., 2015, 2020; Benmammar et al., 2020; Roger et al., 2020; Jacob et al., 2021). Although most recent studies on eclogites integrate a wide variety of data (structural, petrological, geochemical, geochronological, numerical modelling), the interpretation regarding the significance and origin of high-pressure (HP) metamorphism remains in some cases controversial (i.e. Pitra et al., 2021; Whitney et al., 2015, 2020). This uncertainty regarding the tectonic setting associated with HP metamorphism has led to a debate about the number and location of suture zones within the Variscan belt (Kroner & Romer, 2013; Franke et al., 2017; Regorda et al., 2020).

Besides constraining the timing and metamorphic conditions of formation of these eclogites, the next challenge is to decipher from the rock record (mineralogy, structure and microtexture) the processes responsible for the exhumation and the exposure of these HP mafic rocks, which have a higher density than the surrounding crustal rocks (e.g. Schulmann et al., 2008; Whitney et al., 2015, 2020). In the south-western branch of the Variscan belt formed by the Montagne Noire, Corsica-Sardinia and Maures-Tanneron massifs and the Variscan alpine basement (Fig. 1A), eclogites are commonly associated with vertical strike slip shear zones (e.g. Giacomini et al., 2008; Cruciani et al., 2011, 2012, 2015; Whitney et al., 2015, 2020; Trap et al., 2017; Roger et al., 2020; Jouffray et al., 2020; Schneider et al., 2014) and were exhumed throughout various mechanisms such as vertical channel flow in a double gneiss dome (Rey et al., 2011, 2017; Whitney et al., 2015, 2020) or diapirism (Faure & Cottereau, 1988; Soula et al., 2001; Charles et al., 2009). The significance of such eclogite relics within steeply dipping high strain zones remains unclear.

The aim of this study is to decipher the origin of the HP–high temperature (HT) eclogites in the Variscan belt and to constrain their exhumation mechanisms. To this end, we investigated eclogite lenses embedded in migmatitic orthogneisses and affected by a kilometre-scale high-strain dextral shear zone from the Lac Cornu area of the Aiguilles-Rouges Massif (ARM) in the Western Alps (Fig. 1; von Raumer & Bussy, 2004). The tectono-metamorphic evolution is reconstructed by combining forward and inverse thermodynamic modelling (phase diagrams, exchange thermobarometry and Zr-in-rutile thermometry), with geochronology (LA-ICPMS U-Th-Pb dating of zircon, rutile and titanite), geochemistry (whole-rock and zircon trace element composition), and deformation analyses (field-based observations and Electron Backscatter Diffraction (EBSD)). These results give insight into the origin and geodynamic setting of these Variscan HP–HT metamorphic rocks from the ARM and to propose a tectonic model for their exhumation.

2. Geological setting

The Variscan belt resulted from late Paleozoic continental collision between Laurussia and Gondwana continents, preceded by oceanic and continental subduction and possibly by collage of islands arcs and/or continental fragments throughout the late Paleozoic time (e.g. Matte, 1991; Stampfli et al., 2002, 2013; von Raumer et al., 2015; Franke et al., 2017). From North to South, the External Crystalline Massifs (ECMs), comprise the Aar-Gothard, ARM, Mont-Blanc, Belledonne, Pelvoux and Argentera massifs and represent remnants of the Variscan belt. They belong to the para-autochthonous Helvetic domain of the Alps. Alpine deformation and metamorphism are restricted along narrow shear zones with recorded peak metamorphic conditions not overpassing greenschist facies (e.g. Rolland et al., 2003; Rossi et al., 2005; Bellanger et al., 2014; Boutoux et al., 2016).

2.1. Eclogitic occurrences within the ECMs

Several occurrences of mafic lenses or boudins with relict eclogitic assemblages are documented in the ECMs (Fig. 1B; Table 1; e.g. Paquette et al., 1989; Ménot & Paquette, 1993). In the ARM, Belledonne, Pelvoux and Argentera massifs (Fig. 1B; Table 1), these metabasites have mostly a MORB-type geochemical signature. Their protoliths are interpreted as tholeiitic intrusions emplaced within a thin continental crust during continental rifting that may have evolved as far as the opening of a narrow oceanic basin (Paquette et al., 1989; von Raumer et al., 1990; Ménot & Paquette, 1993; Rubatto et al., 2010; Liégeois & Duchesne, 1981). Alternatively, Jouffray et al. (2020) interpreted the geochemical signature of Argentera eclogites as MORBs contaminated by continental crust components, i.e. either basalts from a supra-subduction zone (back-arc basalts) or MORB-type magmas contaminated by crust-derived fluids. In the Aar-Gothard massifs, mafic protoliths have been interpreted as metabasalts with ophiolitic affinity while metagabbros show an island arc affinity (Biino & Meisel, 1993). The protolith ages for the HP mafic rocks of ECMs have been determined by U-Pb on zircon dating (ID-TIMS and LA-ICPMS) between *c.* 483 Ma and 453 Ma (Table 1; e.g. Paquette et al., 1989; Oberli et al., 1994; Rubatto et al., 2001, 2010; Schaltegger et al., 2003; Bussy et al., 2011; Fréville, 2016).

The HP metamorphism occurred at 340.7 ± 4.2 Ma and 336.3 ± 4.1 Ma in the Argentera massif (SHRIMP and ID-TIMS U-Pb on zircon; Rubatto et al., 2010) and ~345 Ma in the ARM (LA-ICPMS on zircon; Bussy et al., 2011). Alternatively, Paquette et al. (1989) suggested the existence of two distinct stages with a 30 Ma gap: the earliest is recorded in the Argentera Massif at ~424 Ma and the second episode in the Belledonne massif at ~395 Ma (eclogite boudins; ID-TIMS U-Pb on zircon). Nonetheless, similar Silurian – early Devonian HP ages and interpretations proposed for the French Central massif are nowadays re-evaluated (Paquette et al., 2017). The range of ages proposed for the HP stage between Ordovician and Visean (Paquette et al., 1989; Abrecht et al., 1991; Rubatto et al., 2010; Bussy et al., 2011; Jouffray et al., 2020) is a source of confusion and constitutes a barrier to the interpretation of the tectonic and geodynamic significance of these eclogites at the scale of the Variscan belt. The pressure–temperature (*P*–*T*) conditions of the HP metamorphism are estimated in the Argentera massif at ~700 °C and 1.4–1.5 GPa (Latouche & Bogdanoff, 1987; Ferrando et al., 2008; Jouffray et al., 2020), in the Belledonne massif at 690–740 °C and 1.4 GPa (Jacob et al., 2021), in the ARM at 650–780 °C and 1.1–1.5 GPa (Liégeois & Duchesne, 1981; Schulz & von Raumer, 1993, 2011), and in the Aar-Gothard massif at ~700–750 °C and 1.8 GPa (Abrecht et al., 1991; Biino, 1994).

In the ECMs, the eclogitic occurrences are mainly interpreted as resulting from continental subduction (Ferrando et al., 2008; Rubatto et al., 2010; Bussy et al., 2011) and are regarded as remnants of dismembered fragments of a suture zone (Abrecht et al., 1991; Jouffray et al., 2020). Recently, Jacob et al. (2021) suggested that HP metamorphism in the Belledonne massif might be induced by crustal thickening of the orogenic crust rather than by oceanic subduction.

2.2. The Aiguilles-Rouges massif

The ARM is an elongated massif striking NNE, composed of a gneissic complex and two Carboniferous synclines (Fig. 1C). The gneissic complex consists of paragneisses and orthogneisses, derived from Ordovician granitoids (von Raumer & Bussy, 2004) that were affected by partial melting. Marble, metabasite and ultramafic rocks occur as lenses in the gneissic complex (von Raumer & Bussy, 2004). The whole sequence is intruded by Carboniferous granites (Bussy et al., 2000). In the ARM, the main Variscan deformation is characterized by dextral transpression forming vertical foliations and large-scale S-C-C' structures (Simonetti et al., 2020a) striking from N150 to N40 (Bellière, 1958). Remnants of ancient planar fabrics are also mentioned, but their tectonic and geodynamic significances are neither discussed nor interpreted (e.g. von Raumer & Bussy, 2004; Joye, 1989). The onset of transpressive deformation was dated at *c.* 320 Ma (U/Pb on monazite, Simonetti et al, 2020a). Zircon and monazite U-Th-Pb ages at *c.* 305 Ma dating the emplacement of ~~on~~ the Vallorcine, Montenvers and Mont-Blanc syntectonic granites are interpreted as the timing of the end of the transcurrent continental deformation (Bussy et al., 2000; Bussy & von Raumer, 1993, 1994).

At least two main metamorphic stages can be distinguished in the ARM: a high pressure and high temperature (HP and HT) stage preserved in eclogites of the Lac Cornu and Val Bérard areas (Fig. 1C; von Raumer & Bussy, 2004). The minimum *P–T* conditions of this HP stage are 780 °C and 1.1 GPa (Liégeois & Duchesne, 1981) and 650–750 °C and 1.25–1.5 GPa (Schulz & von Raumer, 1993, 2011). These eclogitic lenses are surrounded by migmatitic gneisses recording a HT and medium pressure (MP) metamorphism affecting the whole gneissic basement with *P–T* conditions varying from 600–700 °C and 0.4–0.7 GPa (Schulz & von Raumer, 1993, 2011; Joye, 1989; Chiaradia, 2003; Genier et al., 2008; Dobmeier, 1998). Two samples (AR483 and AR481) were collected in a mafic layer near the Lac Cornu (Fig. 2).

3. Methods

3.1. Whole rock and mineral major and trace elements

Major and trace elements data for whole rocks (AR481 and AR483) (Table S1) were obtained using a PANalytical Axios^{mAX} X-Ray Fluorescence (XRF) Spectrometer at the University of Lausanne (Switzerland). Quality control was performed on BHVO2 reference material for trace elements and on BHVO2 and JA-3 references material for major elements.

X-ray maps were acquired using an electron probe microanalyser (EPMA) at the University of Bern (Switzerland) and standardized into maps of oxide weight percentage using an internal standard technique and the program XMapTools 3.4.1 (Lanari et al., 2014; Lanari et al., 2019). Compositional maps of structural formula expressed in atom per formula unit (apfu) were calculated and used to investigate the compositional variability of each mineral phase at the thin section scale. Representative mineral compositions are given in Table S2.

Zr-in-rutile thermometry (Table S3) was also performed using EPMA at the University of Bern following the protocol described in Pape et al. (2016). A knowledge of the pressure of rutile crystallization is required for estimating temperatures at HP conditions (Zhang et al., 2010), therefore we used the thermometer calibration of Tomkins et al., (2007). In order to simplify the description of Zr-in-Rutile thermometer results, we compared temperatures calculated for a fixed pressure of 1.5 GPa; results using other pressure conditions lead to similar results within a temperature range of 650–700 °C. All uncertainties are given at 2σ level. To highlight the possible effects of diffusion on the Zr content of the rutile, we analysed, in both samples, rutile armored by garnet and rutile grains in the mineral matrix that are more likely to re-equilibrate (Zhang et al., 2010). We also avoided rutile partially replaced by ilmenite as it can affect the Zr content in rutile (e.g. Whitney et al., 2015).

Rare Earth Element (REE) analyses on zircon were carried out at the Laboratoire Magmas et Volcans (Clermont-Ferrand, France) with a Thermo Element XR ICP-MS coupled to a Resonetics M-50 laser system operating at a wavelength of 193 nm. Zircon analyses were performed with a spot size of 27 µm, a repetition rate of 3 Hz and a fluency of 2.7 J/cm^2. External calibration was determined relative to NIST 612 glass and internal standard was ^{28}Si. The glass BRC-2G served as secondary standards for data quality control. Data reduction was carried out with the GLITTER® software package (Macquarie Research Ltd 2001; van Achterberg et al., 2001). The REE contents were normalized to the chondritic values of Sun & MacDonough (1989). REE analyses were acquired on the same zone of the dated zircon crystals to infer the geochemical context of zircon crystallization.

3.2. Thermodynamic modelling

Pressure–Temperature phase diagrams were computed in the Na_2O–CaO–FeO–MgO–Al_2O_3–SiO_2–H_2O–TiO_2–Fe_2O_3 (NCFMASHTiO) chemical system using Perple_X 6.9.1. software (Connolly, 2005) and the hpver62 thermodynamic database from Holland & Powell (2011). The solution models used in the calculations were garnet (White et al., 2014); clinopyroxene (Green et al., 2007); amphibole and melt (Green et al., 2016), plagioclase (Fuhrman & Lindsley, 1988), orthopyroxene and chlorite (White et al., 2014), ilmenite (White et al., 2000) and epidote (Holland & Powell, 2011).

For sample AR483, due to relict mineral assemblages, the phase diagrams were calculated using a local bulk composition extracted from the compositional maps using XMapTools (Table S4) (e.g. Duesterhoeft & Lanari 2020). For sample AR481, the bulk rock composition obtained by XRF was used. The H_2O content was refined using a P–$M$$H_2O$ diagram for sample AR483 and by T–$M$$H_2O$ diagram for sample AR481 to reproduce the observed mineral assemblages. In addition, in sample AR483, the Fe^{3+} content was approximated using mineral structural formula of each mineral calculated in XMapTools and their molar concentration in the area analysed. For sample AR481, a T–XFe^{3+} ($XFe^{3+} = Fe^{3+}/Fe_{total}$) diagram emphasizes the growth of epidote in equilibrium with titanite for $XFe^{3+} > 0.2$ and was therefore fixed at 0.1. In this sample, the amount of CaO associated with apatite was removed from the measured bulk composition assuming apatite as the only P-bearing phase.

For sample AR483 we used the mineral compositions extracted from the compositional maps as reference compositions. The P–T conditions of mineral equilibrium were estimated using isopleths and also the *third model quality factor* Q_{cmp} described in Duesterhoeft & Lanari (2020) in order to have a quantitative approach considering more compositional variables. This factor calculates the fitting between the observed and modelled mineral compositions including the relative analytical uncertainty of the measured compositions. The comparison of mineral composition was restricted to CaO, MgO and FeO contents for garnet, of Na_2O, CaO, Al_2O_3, and SiO_2 contents for plagioclase, and of CaO, FeO, MgO, Na_2O, TiO_2, SiO_2, Al_2O_3 contents for amphibole.

The *P*–*T* conditions from local equilibria in sample AR483 were estimated using empirical and semi-empirical thermobarometers implemented in the XMapTools program following the protocol described in Lanari et al. (2013). The *P*–*T* conditions of symplectite were calculated using equilibria involving clinopyroxene, plagioclase, and amphibole (in absence of quartz). The temperature was first estimated from the distribution of Na and Ca between plagioclase and hornblende using the edenite-richterite calibration of Holland and Blundy (1994). Pressure was estimated with fixed composition of amphibole and plagioclase (Table S2) for the defined temperature ranges using the calibration of Waters (2003) based on the reaction jadeite + tremolite = albite + edenite. Temperature conditions of crystallization of amphibole-plagioclase coronae were also estimated using the edenite-richterite calibration of Holland & Blundy (1994).

3.3. U-Pb analyses

Zircon and rutile crystals were obtained by conventional mineral separation. The selected grains (size ~100–200 μm) were mounted in epoxy resin and polished down to expose their near equatorial sections. Rutile and titanite were also analysed in-situ on thin section to preserve the textural relationships between accessory minerals, mineralogical assemblage and the fabric. Before analysis, backscatter electron (BSE) and cathodoluminescence (CL) images were acquired for each grain using a scanning electron microscope (SEM), the locations of LA-ICPMS spot were selected based on the internal microstructures and to avoid inclusions, fractures and other physical defects.

U-Th-Pb isotope data of zircon, rutile and titanite were obtained at the Laboratoire Magmas & Volcans (LMV), Clermont-Ferrand, France by Laser-Ablation Inductively-Coupled Plasma Mass-Spectrometry (LA-ICPMS). The analytical method for isotope dating with LA-ICPMS is similar to that reported in Paquette & Tiepolo (2007), Hurai et al. (2010), and Paquette et al. (2014).

The analyses involved the ablation of minerals with a Resonetics M-50 laser system operating at a wavelength of 193 nm (Müller et al., 2009). The ablated material was carried in helium and then mixed with nitrogen and argon before injection into the plasma source of a Thermo Element XR Sector Field high-resolution ICP-MS. The alignment of the instrument and mass calibration were performed before each analytical session using the NIST SRM612 reference glass, by inspecting the signal of ^{238}U and by minimising the ThO^+/Th^+ ratio (< 1%). Raw data were corrected for U and Pb fractionation during laser sampling and for instrumental mass bias by standard bracketing with repeated measurements of the GJ-1 zircon or Sugluk-4 rutile standards (Jackson et al., 2004; Bracciali et al., 2013). The reproducibility and accuracy of the corrections were controlled by repeated analyses of the 91500 zircon or PCA-S207 rutile standards (Wiedenbeck et al., 1995; Bracciali et al., 2013) treated as unknown (Table S5). For the titanite analyses, owing to a lack of high quality titanite natural standards (i.e. negligible common Pb), zircon standards were used (Table S5). For zircon, rutile and titanite, because of the non-negligible mercury content of the Ar gas creating an isobaric interference between ^{204}Pb and ^{204}Hg, no common Pb correction was applied prior to data reduction using the GLITTER® software package (van Achterbergh et al., 2001). The detailed analytical procedures are presented in the supplementary material (Table S5). The calculated ratios were exported and ages and diagrams generated using Isoplot/Ex v. 2.49 software package (Ludwig, 2001). The decay constants used for the U-Pb system are those determined by Jaffey et al.

(1971) and recommended by the IUGS (Steiger & Jäger, 1977). In the text, tables and figures, all uncertainties are given at 2σ level.

3.4. Microstructures and EBSD analysis

EBSD analyses were performed at Geosciences Montpellier laboratory (University of Montpellier, France) using electron microscopes dedicated to high-resolution crystallographic mapping (JEOL 5600 SEM and CamScan CrystalProbe X500FE), an accelerating voltage of 20 kV and a working distance of 25 mm in “low vacuum” mode. Grid spacing was between 2 and 11 µm in function of the size of the map. All data points that presented misorientation >5° with respect to their eight neighbouring measurements were removed. The EBSD data were reduced using the program Channel 5 from HKL software. “GROD” (Grain Reference Orientation Deviation) filter has been used to illustrate the internal deformation of each mineral. This method provides the average orientation for each grain, and the deviation angle from this mean orientation is then plotted for each pixel (program Channel 5 from HKL software). However, it is dependent on the grain’s detection and division, and thus can be inefficient on small grains. Therefore, local internal deformation was illustrated on small grains by local misorientation maps based on a referential orientation.

4. Results

4.1. Field occurrences of the Lac Cornu eclogites

In the Lac Cornu area**,** mafic rocks form either kilometric-length layers consisting of amphibolite-rich layers or metric to decametric lenses (Fig. 2 and 3A). A mineralogical layering is mainly defined by the different proportion of amphibole, plagioclase and garnet (Fig. 3B). These mafic lenses are surrounded by anatectic orthogneiss and paragneiss. The study area lies within a N-S trending vertical dextral transpressional high-strain shear zone responsible for stretching and boudinage of mafic layers. A vertical pervasive and sometimes mylonitic foliation (S_V, with “v” standing for vertical) dominates in mafic lenses and in the surrounding gneissic rocks (Fig. 2 and 3). Dextral kinematics are inferred from S-C-C’ structures displaying sub-horizontal stretching lineations. Sv is defined by amphibole-plagioclase mineralogical banding and migmatitic layering (Fig. 3C, D and E). A proportion of the melt collected within dilatant structural sites during the stretching and boudinage of the mafic layers (Fig. 3A). In the anatectic gneiss, numerous folds suggest the existence of a previous planar fabric. Based on these observations, this pervasive dextral transpression is interpreted as the main deformation named “D_V” forming a “S_V” foliation and dextral S_V-C_V-C_V’ structures.

Locally, D_V low-strain domains preserve relics of a previous planar fabric. This fabric forms a sub-horizontal foliation (S_H, with “H” for horizontal) that is folded by S_V (Fig. 2, 3C to 3E). High-strain associated with S_V does not allow us to investigate in greater detail the original orientation and the kinematics of D_H deformation. In gneisses, the S_H foliation is defined by a migmatitic layering also indicating a suprasolidus origin. In mafic boudins, S_H is recognized by the mineralogical banding (Fig. 3B) where clinopyroxene is still visible, indicating pressure conditions higher than the clinopyroxene amphibole-free assemblage of the S_V foliation.

Within the D_V shear zones, eclogites are extensively retrogressed into amphibolites (Fig. 3; e.g. von Raumer & Bussy, 2004; Liégeois & Duchesne, 1981). Eclogite facies paragenesis and more particularly clinopyroxene-bearing assemblages are best preserved within the S_H foliation in low- D_V strain domains (Fig. 3). Both samples (AR483 and AR481) were collected in a 50 meter-thick mafic layer (Fig. 2). Sample AR483 (N45°57’36’’; E06°50’42’’) is a well-preserved eclogite collected as a boulder in the eclogitic area. The S_H foliation is defined by the mineralogical layering with clinopyroxene-bearing assemblages. Sample AR481

(N45°57’33’’; E06°50’47’’) is a more retrogressed eclogite than the sample AR483 and is collected in an amphibolite facies D_V shear zone with a vertical S_V foliation mainly composed of amphibole and plagioclase (Fig. 3C).

4.2 Bulk composition of eclogites

Major and trace element contents from samples AR483 and AR481 are similar (Table S1). In the total Alkali versus Silica diagram (Le Bas et al., 1986) (Fig. S1A), the two samples plot in the basalt field (2.85 and 2.63 wt% Na2O+K2O, and 50.05 and 51.71 wt% SiO2), with the sample AR481 near the basaltic andesite field. In the AFM diagram (Irvine & Baragar, 1971), they belong to the tholeiitic series (Fig. S1B). Samples AR483 and AR481 have typical N-MORB compositions (Fig. S1C) with a tholeiitic to andesitic basalt affinity (Fig. S1C and D; Meschede, 1986; Pearce, 1996). In the Al_2O_3 vs TiO_2 diagram (Konzett et al., 2012), both samples plot in the basalt field (Fig. S1E). These compositions are similar with published data from the ARM (see white circle, black and grey dots on Fig. S1; Paquette et al., 1989; von Raumer et al., 1990; Liégeois & Duchesne, 1981).

4.3. Petrology and mineral compositions

4.3.1. Weakly retrogressed eclogite AR483

Sample AR483 is a weakly retrogressed eclogite composed of amphibole, garnet, clinopyroxene, plagioclase, quartz, with minor rutile, ilmenite, apatite, zircon and epidote (Fig. 4A). Two mineralogical layers are recognized based on the amount of quartz (Fig. 4A): quartz-rich layers are associated with symplectites whereas quartz-poor layers are composed of large clinopyroxene and amphibole grains. Mineralogical layering and preferential orientation of amphibole and clinopyroxene define the S_H foliation. Clinopyroxene occurred as coarse grains often partially retrogressed into clinopyroxene-plagioclase-bearing symplectites (Fig. 4A).

Clinopyroxene shows a variable composition with the jadeite content ranging from 35 mol% to 11% depending on the textural location (Fig. 5B; Table S2). Clinopyroxene included in garnet is omphacite with jadeite content of 31–35% (Cpx_1). Omphacite is also present in the matrix as relict compositionally zoned and partially recrystallized into amphibole (Fig. 5B). The breakdown of Cpx_1 involves the formation of sodic-poor clinopyroxene (Cpx_2) in symplectite. Clinopyroxene compositions from the symplectites (Cpx_2) vary between 25 and 11 mol% of jadeite (Fig. 5B).

Garnet is sub-euhedral and grain size ranges from 2 to 15 mm in diameter. It contains abundant inclusions of quartz, rutile, zircon, apatite and omphacite (Cpx_1) and scarce inclusions of epidote and small amphibole. Garnet exhibits compositional zoning with a large Ca-rich core (Grt_1) ($Alm_{52}Prp_{21}Grs_{24}Sps_1$), and a thin Ca-poor, Fe- and Mg-rich overgrowth (Grt_2) ($Alm_{55}Prp_{24}Grs_{17}Sps_1$) (Fig. 5C and D). Garnet cores (Grt_1) show an euhedral shape without significant variation in chemical composition or zoning (Fig. 5D). The transition between core Grt_1 and overgrowth Grt_2 is sharp (Fig. 5C and D). Garnet overgrowths (Grt_2) are better developed when in contact with the symplectite (Fig. 5C), which suggests that Grt_2 and Cpx_2-symplectite formed at the same time.

Amphibole occurs in two distinct textural positions: amphibole associated with clinopyroxene (Cpx_2)–plagioclase-bearing symplectites and amphibole associated with plagioclase in coronas surrounding garnet overgrowths (Grt_2) (Fig. 5A). Although both types of amphibole have different compositions they are referred to $Amph_2$. Amphibole in the Cpx_2-symplectites is homogeneous in composition and corresponds to magnesio-hornblende (Leake et al., 1997). Amphibole in coronae shows zoning with XMg and Si apfu varying from 0.60 and 6.48 to 0.63 and 5.75, respectively (Fig. 5E) (Table S2). It evolves from a ferroan-pargasite in contact with garnet to tschermakitic-hornblende (Leake et al., 1997) away from the garnet contact.

Plagioclase (Pl_2) from the matrix, symplectite and corona is homogeneous in composition with an albite content varying from 87 to 89 mol% (Fig. 5F; Table S2). Rutile and zircon are present in the matrix-and rutile is partly replaced by ilmenite.

4.3.2. Strongly retrogressed eclogite AR481

Sample AR481 is a retrogressed eclogite composed of amphibole, plagioclase, quartz, garnet, it also contains minor clinopyroxene, titanite, ilmenite, rutile, zircon, apatite and magnetite as relics or accessory minerals (Fig. 4B). Omphacite is absent. Clinopyroxene-plagioclase symplectites are replaced by large euhedral magnesio-hornblende ($Amph_3$) and plagioclase (Pl_3) with lower albite content (62 mol%; Table S2). Garnet compositions and chemical zoning (Table S2) are similar to those observed in sample AR483. Garnet shows resorption textures at the expense of the plagioclase-hornblende corona and is sometimes totally replaced by plagioclase and amphibole (Pl_3 + $Amph_3$). Euhedral amphibole in the matrix has XMg and Si apfu of 0.60 and 6.56 (Table S2). Rutile is partially replaced by lamellae and patches of ilmenite, and both phases breakdown into titanite forming coronas (Fig. 4B). Magnetite is present in fractures of the sample and does not show clear relationships with other minerals.

4.3.3. Petrological interpretations

Three main mineral assemblages corresponding to three metamorphic stages M1, M2 and M3 are inferred from the petrological observations.

(1) The earliest stage M1 corresponds to the garnet core (Grt_1) and its inclusions (Cpx_1 + Qtz + Rt + Ap ± Ep ± Amph).

(2) The M2 stage can be subdivided into the formation of two assemblages M2a and M2b. The M2a assemblage is associated with the development of garnet (Grt_2) overgrowths concurrent with the formation of Cpx_2-Pl_2-$Amph_2$-symplectites replacing omphacite (Cpx_1). The M2b

stage is characterized by the development of $Amph_2$-Pl_2 corona around garnet and by the breakdown of rutile into ilmenite. The progressive decrease of jadeite content within Cpx_2 suggests that symplectites developed progressively from M2a to M2b.

(3) The third stage M3 is marked by large amphibole crystals and plagioclase replacing garnet and clinopyroxene-plagioclase symplectites ($Amph_3$ + Pl_3). Ilmenite and rutile breakdown into titanite.

4.4. Crystallographic preferred orientations (CPO)

To establish the relationships between the three metamorphic stages M1, M2, M3 and deformation (i.e. D_H and D_V), the CPO of each mineral assemblage was investigated. The CPO are plotted in the structural reference frame of the sample, where X-, Y- and Z- axes correspond to the three principal directions of the strain ellipsoid of either S_H or S_V planar fabrics. The main planar fabric in sample AR483 is the S_H foliation defined by compositional layering and preferential alignment of matrix minerals (Fig. 6). Clinopyroxene in the matrix (i.e. Cpx_1 and Cpx_2) is characterized by the alignment of {010} planes parallel to the S_H foliation. The C-axis <001> defines a girdle with a maximum close to the stretching lineation (Fig. 6E). The D_H stretching direction is also defined by the orientation of rutile C-axis <100> (Fig. 6E). Omphacite and rutile included in garnet do not display the same CPO as in the matrix. Omphacite (Cpx_1) armoured in garnet CPO shows a single point maximum of {100} poles and a poorly defined girdle C-axis <100> CPO. Quartz included in garnet or located in the matrix does not show a preferential orientation (Fig. 6E). The GROD map of clinopyroxene (Fig. 6B) indicates that clinopyroxene in symplectite has only internal misorientations inferior to 1° suggesting an absent or weak plastic deformation (Fig. 6C). Local misorientation map on clinopyroxene in late fine-grained symplectites highlights a weak plastic deformation (Fig. 6D).

Sample AR481 shows a mylonitic foliation S_V and is nearly totally retrogressed into amphibolite (Fig. 7A). A large EBSD map from this sample indicates that amphiboles have low internal misorientation, mostly inferior to 1° (Fig. 7A and B). The CPO of amphibole indicates that {100} planes are parallel to the main S_V mylonitic foliation and C-axis <001> defines a girdle parallel to the S_V foliation (Fig. 7C). Titanite has very weak CPO (Fig. 7C), nonetheless, its C-axis <001> presents a broad orientation perpendicular to the S_V foliation.

4.5. Thermodynamic modelling

4.5.1. Peak pressure record (eclogite AR483)

In this sample (AR483), the M1 stage is defined by garnet core composition and its inclusions (Cpx_1 + quartz + rutile) and omphacite (Cpx_1) within the matrix. Scarce epidote and amphibole inclusions in garnet cores (Grt_1) indicate that the rock was not fully dehydrated during the crystallization of the garnet cores. The amount of H_2O was investigated through P–MH$_2$O and T–MH$_2$O phase diagrams (Fig. S2A and B). These diagrams indicate that an amount of *c.* 0.4 wt% of H_2O is necessary to crystallize epidote during prograde metamorphism. At higher H_2O content, rutile is replaced by titanite. The absence of titanite inclusions in garnet cores and the presence of numerous inclusions of rutile suggest H_2O undersaturated conditions for the M1 stage.

The Grt + Cpx + Rt + Qtz mineral assemblage is observed at pressures above the stability field of plagioclase with additional phases (Ttn, Ep, Amph, H_2O or melt) (Fig. 8A). Measured grossular, almandine and pyrope isopleths of Grt_1 and jadeite isopleth of Cpx_1 intersect at ~ 710 °C and 1.75 GPa (Fig. 8A) in the stability field of Cpx + Grt + Amph + Rt + H_2O, which is consistent with the observed garnet inclusions (compositions used for minerals isopleths are summarized in Table S2). Considering analytical uncertainties from Grt_1 composition, the Q_{cmp} factor reaches 100% between ~ 650–750 °C and 1.70–1.95 GPa and at ~ 780 °C and 1.53 GPa

(Fig. 8B). The *P–T* conditions at 650–750 °C and 1.70–1.95 GPa are also consistent with the observed jadeite content of Cpx_1. Therefore, *P–T* conditions defined by the Grt_1 and Cpx_1 isopleths at ~ 710 °C and 1.75 GPa are interpreted as the conditions of the M1 stage.

The *P–T* phase diagram shown in Figure 8A indicates that epidote was not stable at the M1 conditions whereas it is predicted to be stable at lower *P–T* conditions. This suggests that epidote could be the only relict of the prograde stage. However, because the epidote stability is strongly dependent on Fe_2O_3 and H_2O content, that are difficult to quantify with confidence, the prograde *P–T* path is not constrained.

4.5.2. Retrograde path of weakly retrogressed eclogite AR483

The M2 stage consists of Grt_2 + Cpx_2 + $Amph_2$ + Pl_2 + Qtz + Rt/Ilm. The amount of H_2O required to stabilize amphibole was investigated through a *P–M*H_2O diagram (Fig. S2C). The best estimate of H_2O content is again constrained at *c*. 0.4 wt% to avoid the stability of orthopyroxene at low-water content and titanite at higher-water content.

The computed phase diagram is shown in Figure 9A. The M2a mineral assemblage (Grt + Cpx + Amph + Pl + Qtz + Rt) is predicted to be stable at temperatures below 850 °C for a pressure of 1.6 GPa. Between 750 °C and 850 °C, melt is expected. Considering the mineral assemblage and the grossular, almandine and pyrope isopleths of the Grt2 (compositions in Table S2), the best *P–T* estimate (Q_{cmp} factor = 100%) for M2a are ~ 800 °C and 1.50 GPa (Fig. 9A and B). The highest jadeite content isopleth of Cpx_2 (XJd = 25 mol%; Table S2) is also consistent with these *P–T* conditions (Fig. 9A). Considering the Cpx_2-symplectite and Grt_2 equilibrium observed in this sample, we propose the conditions of 800 °C and 1.50 GPa for the stage M2a.

The M2b stage is characterized by the replacement of rutile by ilmenite, and the formation of Pl_2-$Amph_2$-coronae around garnet. The crystallization of ilmenite at the expense of rutile and the decrease of jadeite content in the Cpx_2 are consistent with a decompression down to ~ 0.80–0.90 GPa (Fig. 9A). The lack of orthopyroxene constrains the maximum temperature of the M2b stage at 775 °C. The highest values of Q_{cmp} factor for $Amph_2$ in the symplectite and in the corona (80% and 70% respectively) indicate pressure conditions between 0.9 and 1.1 GPa (Fig. 9C and D). These pressure conditions are also consistent with the Cpx_2 jadeite content (11% to 25%) (Fig. 9C and D). These relatively poor Q_{cmp} values (80% and 70%) may be related to uncertainties in the thermodynamic models (Duesterhoeft & Lanari, 2020) or the effects of local equilibrium for which the selected reactive bulk composition becomes inappropriate (Lanari & Engi, 2017).

4.5.3. Strongly retrogressed eclogite AR481

Sample AR481 is characterized by the replacement of clinopyroxene and garnet by amphibole ($Amph_3$) and plagioclase (Pl_3) and rutile by ilmenite. The increase in amphibole mode requires the addition of H_2O prior or during the M3 stage. The P–$M$$H_2O$ diagram, shown in Figure 10A, suggests that the mineralogical evolution observed requires an increase of the water content from at 0.4 wt% to at least 1.6 wt%. In the sample AR481, during the final retrograde stage, ilmenite and remnants of rutile are replaced by titanite and minor chlorite crystallized in garnet fractures. The amount of H_2O required to stabilize this final paragenesis, without the crystallization of epidote, was constrained to between 1.6 and 2.5 wt% at LT–LP conditions (Fig. S2D). To conclude, the retrogression of eclogite into amphibolite is characterized by an increase of H_2O content all along the retrograde path from ~0.4 to 2.5 wt%.

The phase diagram shown in Figure 10B, has been computed with a H_2O content of 2.4 wt%. The mineral assemblage Amph + Pl + Qtz + Ilm forms a large stability field ranging between ~525–775 °C and 0.35–0.90 GPa (less than 0.20 GPa if we include the stability field with a second amphibole). If we consider the $Amph_3$ composition, the highest Q_{cmp} factor (70%) is obtained between ~630–715 °C and 0.22–0.34 GPa (Fig. 10C; Table S2). These conditions are consistent with the stability of Ca-Amph + Fe-Amph + Grt + Pl + Qtz + Ilm. Q_{cmp} factor of the Pl_3 composition reaches 100% in the stability field of Amph + Grt + Pl + Ilm + Qtz from ~ 700 °C and 0.85 GPa to 580 °C and 0.40 GPa (Fig. 10D; Table S2). The combination of Pl_3 and $Amph_3$ best *P*–*T* estimates roughly define HT–LP conditions at ~650–700 °C and 0.20–0.60 GPa. The last stage of M3 metamorphism corresponds to the appearance of titanite at *P*–*T* conditions below 500 °C and 0.5 GPa.

4.5.4. Empirical thermobarometry of local equilibria

Temperatures of the Cpx_2–$Amph_2$–Pl_2 symplectite in sample AR483, were estimated with the amphibole–plagioclase thermometer of Holland & Blundy (1994) and range from 550 °C to 770 °C (Fig. 11A). The clinopyroxene–hornblende–plagioclase thermo-barometer of Waters (2003) was used with two distinct compositions of amphibole located in the symplectite ($Amph_2$ symplectite in Table S2) and a fixed composition of plagioclase (Pl_2, Table S2). Our results show that the symplectite crystallized at *P*–*T* conditions ranging from ~1.65 GPa and 765 °C to ~1.0 GPa and 625 °C for both amphibole compositions (n = 302313; Fig. 11A). These *P*–*T* conditions are consistent with plagioclase stability modelled with the bulk composition of sample AR483 with garnet cores excluded (Fig. 9). Both *P*–*T* conditions carried out via forward and inverse modeling are consistent (Fig. 9 and 11).

4.5.5. Zr-in-rutile trace element thermometry

One hundred and twenty analyses were performed on 80 rutile crystals from samples AR483 and 40 rutiles from AR481 (Table S3). In the weakly retrogressed eclogite (AR483), Zr contents of rutile inclusions in garnet vary between 245 and 566 ppm with a mean value of 421 ppm and a standard deviation of 162 ppm (2σ, n = 27). Zr contents of matrix rutile range from 309 to 644 ppm with a mean value of 435 ppm and a standard deviation of 126 ppm (2σ, n =

53). The estimated temperature values for rutile inclusions in garnets (n= 27) and matrix rutile (n= 53) range between 655 °C to 726 °C and between 673 °C to 739 °C, respectively (Fig. 11C, Table S3) with mean temperatures of 698 ± 36 °C (n = 27) and of 702 ± 26 °C (n = 53) for rutile inclusions and matrix rutile, respectively. The histogram of Zr-in-rutile temperature shows modal and similar distributions for the two populations (i.e. rutile inclusions and matrix-rutile grains) centred around ~700–710 °C (Fig. 11C). All of these data yield a mean temperature of 701 ± 30 °C (n= 80).

For the strongly retrogressed eclogite (AR481), the Zr contents of rutile inclusions range between 280 and 582 ppm with a mean value of 376 ppm and a standard deviation of 170 ppm (n = 16). Zr contents of matrix rutile vary between 356 ppm and 729 ppm with a mean value of 503 ppm and a standard deviation of 156 ppm (n = 24). Estimated temperatures for the inclusion rutile (n=16) range between 665 °C and 729 °C (Fig. 11D). A histogram of Zr-in-rutile temperature for inclusion rutile shows a bimodal distribution with a high temperature peak at ~695 °C and a low temperature peak at ~670 °C (Fig. 11D). The low temperature group composed by six analyses has a mean temperature of 670 ± 6 °C while the group at higher temperature (except one analysis at 729 °C), yields an average temperature of 696 ± 20 °C (n=9). The twenty-four analyses obtained on matrix rutile yield temperatures ranging from 685 °C to 750 °C with a mean temperature of 715 ± 28°C.

4.6. U-Th-Pb geochronology

4.6.1. Zircon dating

The zircon crystals from both samples are transparent and colourless. Zircon ranges in shape from rounded to sub-euhedral, equant to elongate and some grains are multi-faceted typical of HP rocks. CL images show prismatic crystals characterized by oscillatory zoning and rounded edges reflecting probably the magmatic growth of the crystals and rounded crystals with an irregular, chaotic and patchy zoning often described in HP zircons (Corfu et al., 2003). A few grains show cores, which are dark in CL with patchy or sector-like zoning or oscillatory zoning and rims, which are bright and featureless in CL (Fig. 12A and B).

4.6.1.1. Weakly retrogressed eclogite AR483

Seventy-five analyses were performed on fifty-nine zircons (Table S6). In a concordia diagram, the two distinct populations of zircon can be distinguished around *c.* 460 Ma and *c.* 330–340 Ma (Fig. 13A). The major and oldest population is characterized by low to medium Pb (3.2–20 ppm), U (44–247 ppm) and Th (most 7.6–55 ppm) contents with Th/U ratios in the range 0.14 to 0.46. It consists essentially of cores with oscillatory zoning and a few CL-dark rims (Table S6; Fig. 12A). Fifty-five data yield a concordia age of 461.6 ± 1.2 ($MSWD_{(C+E)}$ = 1.02) (Fig. 13A). The youngest population (ca. 330 Ma) is constituted by eleven data performed on two zircon rims (Zr59 and A11/Zr3), bright and featureless in CL and on three grains likely neoformed (Zr23, Zr63 and Zr52) (Fig. 12A). Except for one (Zr63), these analyses have very low to low Pb (0.9– 2.4 ppm), U (18–49 ppm) and Th (most 0.1–1.8 ppm) contents and low Th/U ratios (< 0.01) (Table S6). Among these, ten analyses yield a concordia age of 337.3 ± 4.7 Ma ($MSWD_{(C+E)}$ = 2.2). The discordant position of the analysis obtained for the CL-bright rim of zircon Zr59 (dashed line) is probably due to common-Pb contamination. The three concordant ellipses around *c.* 440 Ma (Zr27), 390 Ma (Zr19) and 365 Ma (Zr15) may correspond to a mixture between the Ordovician component (460 Ma) and the Variscan component (330–340 Ma).

4.6.1.2. Strongly retrogressed eclogite AR481:

Sixty-eight analyses were carried out on fifty-three zircons (Table S6; Fig. 13B). The results are very similar to those obtained on zircon of the sample AR483. The data form a cluster around 460 Ma. These analyses of cores and rims are characterized by low to medium Pb (most

2.7–22 ppm), U (most 37–287 ppm) and Th (most 6.2–52 ppm) contents with Th/U ratios in the range 0.12 to 0.27. Sixty-one analyses yield a concordia age of 461.7 ± 1.6 Ma ($MSWD_{(C+E)}$ = 1.09, n = 61) (Fig. 13B). Only analyses obtained on the CL-bright rim of zircon Zr29 yielded young date at 334 ± 12 Ma (n = 3) using a lower intercept (Fig. 11B and 12B). This rim has very low to low Pb (1.3–1.4 ppm), U (27–30 ppm) and Th (0.1–0.3 ppm) contents and low Th/U ratios (< 0.01).

4.6.2. Rutile dating

Rutile of both dated samples shows euhedral to anhedral forms with a reddish color. Each grain is generally unzoned in BSE images, with no indication of preservation of more than one generation. Rutile of the sample AR481 analysed in situ on a thin section (AR481c) forms mainly crystals in the matrix composed of amphibole, plagioclase and quartz, but also occurs as inclusion in garnet (Fig. 12C and D). Matrix rutile has titanite-coronae. The eclogitic samples have rutile with low U contents between 0.5 and 20 ppm and very low Pb contents of 0.02–0.5 ppm (Table S6).

4.6.2.1. Weakly retrogressed Eclogite AR483:

Fifty-one separate rutile crystals (100–200 µm size) were analysed. In a Tera-Wasserburg diagram, the ellipses plot in concordant to discordant position according to the various proportions of common Pb compared to the radiogenic Pb. The linear regression using all data yields a lower intercept date of 330.1 ± 1.7 Ma (MSWD = 0.55, n = 51) and forty-four of these data give an equivalent concordia age of 330.6 ± 1.8 Ma ($MSWD_{(C+E)}$ = 1.02; n = 44) (Table S6; Fig. 13C).

4.6.2.2. Strongly retrogressed eclogite AR481 and AR481c

Nineteen separate crystals were dated (Table S6). Most of the data are close to the concordia curve, in the Tera-Wasserburg diagram (Fig. 13D). The linear regression using entire dataset gives a lower intercept date of 326.6 ± 3.3 Ma (MSWD = 0.41; n = 19). Twelve among these data yield a concordia age of 328.3 ± 3.7 Ma ($MSWD_{(C+E)}$ = 1.14).

Twenty spots on thirteen rutile grains were also analysed in situ on a thin section (AR481c). Among these analyses, eight were performed on eight crystals included in the garnet and yield a lower intercept date of 340.0 ± 8.6 Ma (MSWD = 0.34; n=8) (Fig. 13E; pink ellipse). Twelve spots were carried on five rutile crystals located in the mineral matrix. In the Tera-Wasserburg diagram, these ellipses are generally less discordant than those obtained on rutile included in garnet (Fig. 13E). The linear regression yields a lower intercept date of 339.9 ± 4.2 Ma (MSWD = 0.43; n=12) and five give a concordia age of 342.5 ± 8.0 Ma ($MSWD_{(C+E)}$ = 1.8). All these dates obtained on rutile included in garnet or in the matrix are similar within the uncertainties. The dataset obtained on 32 rutile grains (separate, inclusion and matrix) yield a lower intercept date of 331.7 ± 2.3 Ma (MSWD = 1.2; n = 39) and among these data, seventeen give a concordia age of 332.6 ± 4.0 Ma ($MSWD_{(C+E)}$ = 1.9) which is identical within uncertainty to the concordia age of 330.6 ± 1.8 Ma ($MSWD_{(C+E)}$ = 1.02; n = 44) obtained on the rutiles of the sample AR483.

4.6.3. Titanite dating

Nineteen analyses on seventeen titanite crystals were also analysed in situ on a thin section (AR481c). Part of the analysed titanite takes the form of a corona texture around rutile (Fig. 12C; Table S6).

Titanite has very low contents of U (1–4.6 ppm) and Pb (< 2 ppm) with low Th/U ratios (<1) (Table S6). The uncorrected data are plotted in the Tera–Wasserburg diagram (Fig. 13F), and a linear regression through all these analyses forms a lower intercept that yields a date of 297.6 ± 9.8 Ma (MSWD = 0.71; n = 19). The y-intercept of 0.872 ± 0.009 represents the initial

$^{207}Pb/^{206}Pb$ (Aleinikoff et al., 2002), which can be used for common Pb correction (Stern, 1997; Frost et al., 2000). This value is in a relatively good agreement with the Stacey & Kramers (1975) terrestrial Pb evolution model (0.86 at 300 Ma). Subsequently, the individual ^{207}Pb-corrected $^{206}Pb/^{238}U$ dates can be calculated and yield the weighted average of 297 ± 1 Ma (MSWD = 2.1; n = 19), consistent with the lower intercept date within the error range.

4.7. U-Th-Pb geochronology

Fourteen trace element analyses were carried out on nine and two zircons for samples AR483 and AR481, respectively (Fig. 14; Table S7). The chondrite-normalised REE patterns of the zircon from these two eclogites are similar and exhibit two distinct populations of spectra according to the obtained ages. The first population is constituted by seven Ordovician cores (~455–460 Ma) and one core dated at *c.* 364 Ma. It is characterised by a steeply-rising slope from the Light REE (LREE) to heavy REE (HREE), in particular with a strong variable enrichment in heavy REE (HREE) with respect to middle REE (MREE) (Lu_N/Sm_N = 219–1038), and with a positive Ce anomaly (25.3–79.9) and a moderate negative Eu anomaly (0.64–0.78) (Fig. 14A). The total REE abundances are ranging between 184 ppm and 340 ppm with low LREE contents around 2 ppm (Table S7). The Variscan population consists mainly of zircon rims dated at *c.* 330 Ma as well as two analyses dated to *c.* 390 Ma. It shows lower total REE contents (27–159 ppm). It displays a weaker enrichment in HREE with respect to MREE (most Lu_N/Sm_N= 10.7– 59) but with a flat HREE pattern (most Lu_N/Dy_N = 1.64–4.35) at 30–110 times chondrite, with a positive anomaly in Ce (3.9–36.4) and no Eu anomaly (0.92–1.08) (Table S7; Fig. 14B).

5. Discussion

5.1. P–T–D–t path of the ARM eclogites

Mineralogical and structural analyses coupled with thermodynamic modelling, geochronology and microstructural analyses allows the retrograde *P–T–D–t* evolution of the Lac Cornu eclogites to be reconstructed (Fig. 15A).

5.1.1. The high-pressure stage (M1)

Eclogitic facies M1 stage is defined by the Grt_1 + Cpx_1 + Qtz + Rt mineral assemblage. The Grt_1 and Cpx_1 compositions yield *P–T* conditions at 710 °C and 1.75 GPa (Fig. 8). The presence of a few epidote inclusions in garnet core indicates that garnet could have started to grow during the prograde path. However, garnet composition and zoning do not preserve chemical evidences of this prograde path, which were very likely overprinted by chemical diffusion at high-grade conditions (e.g. Yardley, 1977; Tedeschi et al., 2017).

Rutile crystallized at high-pressure conditions (Fig. 8). Rutile included and armoured Grt_1 cores yield slightly lower temperatures, between 650 to 730 °C, interpreted as the temperature of crystallization of rutile during the prograde M1 metamorphic evolution (Fig. 11B and C). In the most retrogressed sample (AR481), Zr-in-rutile thermometry of rutile in the matrix yields consistent temperatures though slightly higher from 680 °C and up to 750 °C (Fig. 11C). Considering a M1 peak pressure of 1.8 GPa with all the Zr-in-rutile temperatures, we obtain an average temperature for pressure peak of 701 ± 30 °C similar within uncertainties to those obtained by forward phase relation modelling (Fig. 15).

Geochronology on separated rutile grains, from samples AR483 and AR481, yield concordia ages of 330.6 ± 1.8 Ma and 328.3 ± 3.7 Ma respectively (Fig. 13C and 13D). In the strongly retrogressed eclogite AR481, in-situ dating of rutile included in garnet yields a similar age of 332.6 ± 4.0 Ma (Fig. 13E). We interpret these dates as the peak pressure age. Both eclogite samples contain zircon rims and neoformed crystals with very low Th/U ratios (<0.01), a lack of Eu anomalies, and only weakly enriched in HREE with respect to MREE with a flat HREE spectrum. These characteristics suggest zircon grew in equilibrium with a garnet-bearing and plagioclase-free assemblage under eclogite facies conditions (Rubatto, 2017). Metamorphic zircon from eclogite samples AR483 and AR481 yield a concordia age of 337.3 ± 4.7 Ma and a lower intercept date of 334 ± 12 Ma, respectively (Fig. 13A and B), both interpreted as the age of the peak pressure. In summary, U-Pb dating of zircon and rutile provides a reliable timing of HP metamorphism in the ARM between 330–340 Ma.

EBSD results obtained on the weakly retrogressed eclogite (AR483) highlight different CPO between matrix minerals and inclusions in garnet. We interpret this result as evidence of deformation prior to D_H recorded by the Cpx_1 and rutile armoured in the garnet cores, and unrecognized at the macro-scale on the field. We speculate that this deformation is related to crustal thickening, and possible nappe stacking, that took place contemporaneously with prograde metamorphism and before the pressure peak at 330–340 Ma (Fig. 15A).

5.1.2. Onset of the decompression (M2)

The onset of the decompression path (stage M2) is highlighted by the growth of Grt_2 rims, Cpx_2–Pl_2–Amph symplectites and rutile breakdown to ilmenite (Fig. 9 and 15). This decompression is also emphasized by the progressive decrease of jadeite content in Cpx_2 (Fig. 5B). Grt_2 and Cpx_2 compositions indicates *P–T* conditions of ~800 °C and 1.5 GPa (Fig. 9) interpreted as conditions of the early stage of decompression temperature in suprasolidus conditions. Thermobarometry applied on Cpx_2 and $Amph_2$ indicates a progressive pressure decrease from ~1.6 to 0.9 GPa. Combining all these data, we propose that the decompression from 1.6 to 0.8 GPa occurred at temperatures between 650 and 775 °C (Fig. 9 and 11A). The preservation of garnet zoning may suggest that the rocks were not exposed to the high-temperature conditions for a long time (e.g. O'Brien, 1997).

EBSD results on sample AR483 indicate that clinopyroxene in symplectites (Cpx_2) is weakly plastically deformed. We suggest that symplectite growth was contemporaneous with D_H deformation active during the onset of decompression. Therefore, we suggest that the development of the sub-horizontal S_H along the decompression path occurred during unroofing of lower crustal material. In the gneissic basement, the sub-horizontal S_H foliation is associated with widespread anatexis, suggesting that D_H could be associated with horizontal flow of the lower anatectic crust (e.g. Beaumont et al., 2001; Vanderhaeghe, 2009; Rosenberg et al., 2007) that began after the peak of pressure at *c.* 330–340 Ma.

5.1.3. Late exhumation stage (M3)

The most retrogressed mafic boudins (AR481) consist of plagioclase (Pl_3) + amphibole ($Amph_3$) + quartz + ilmenite + titanite ± chlorite (Fig. 4B) predicted to be stable below 500 °C and 0.5 GPa, suggesting that the ARM was affected by a late HT–LP metamorphism (Fig. 10~~B~~). Although the Q_{cmp} factor of Amph3 is low (i.e. 0.70%), we consider this result as meaningful because similar *P*–*T* conditions have already been obtained on metasedimentary rocks of the ARM (Genier et al., 2008; Chiarada, 2003). Furthermore, HT–LP metamorphism has also been identified in the north-eastern ARM (Fully area, Fig. 1C) with cordierite-bearing migmatites (Krummenacher, 1959; Bussy et al., 2000).

The CPO of amphibole ($Amph_3$) in sample AR481 is consistent with high-temperature (>600 °C) and low-stress conditions (Ko & Jung, 2015) during an active shearing (e.g. Ko & Jung, 2015; Kim & Jung, 2019; Getsinger & Hirth, 2014). Furthermore, CPO of titanite also indicates crystallization during active shearing (Papapavlou et al., 2017). Therefore, crystallization of $Amph_3$ and titanite are coeval with D_V shearing. Titanite exhibits low U and Pb contents with high proportion of common Pb, resulting in a large uncertainty on the calculated age. Moreover, Sun et al. (2012) demonstrated that titanite can be up to ~12 % younger than their known ages using either spot or raster analyses when a zircon standard is used, so we cannot completely rule out that this lower intercept age could be younger than the titanite crystallization age. Thus, the lower intercept date (297.6 ± 9.8 Ma) is interpreted as a minimum age of the crystallization age of titanite. Nonetheless, this age at *c.* 300 Ma is consistent with Ar/Ar radiogenic ages at *c.* 300 Ma obtained on muscovite from gneissic boulders in the Salvan-Dorenaz syncline (Capuzzo et al., 2003). Therefore, titanite crystallization at conditions below 500 °C and 0.5 GPa (Fig. 10) was synchronous with the D_V deformation and the latest stage of exhumation of the ARM at ~300 Ma (Fig. 13F). This timing also corresponds to the emplacement of the Vallorcine and Mont-Blanc granites during the dextral (D_V) shearing deformation at *c.* 305 Ma (Bussy & von Raumer, 1993, 1994; Bussy et al., 2000). Since the dextral shearing began at suprasolidus conditions (Genier et al., 2008; von Raumer & Bussy, 2004) with the crystallization of anatectic melt starting to occur at 320 ± 1 Ma (Bussy et al., 2000), a minimum duration of the dextral transpressional shearing stage of 20 Ma is proposed for the ARM (Fig. 15A). It is very likely that the transition between D_H lateral flow and D_V dextral shearing was progressive and that they were spatially partitioned during a single transpressive regime. This M3 HT–LP metamorphism is also dated at *c.* 305 Ma by the synchronous emplacement of the Crd-bearing Vallorcine pluton and Fully Crd-bearing migmatites (Bussy et al., 2000).

5.2. Significance of HT eclogites—are the eclogites of the ARM part of a suture zone?

Two main geodynamic mechanisms are proposed to explain the HP conditions reached by mafic rocks in the Variscan belt: (i) subduction-related eclogite, associated to either oceanic subduction (e.g. Jouffray et al., 2020; Bellot et al., 2010; Schneider et al., 2014; Lardeaux et al., 2001; Berger et al., 2010) or continental subduction (e.g. Giacomini, Braga, Tiepolo, Tribuzio, 2007; Miller & Thöni, 1995; Lotout et al., 2020) and (ii) continental crust thickening allowing material located at the roof of the crust to reach eclogitic conditions through horizontal compression and lateral flow (e.g. Whitney et al., 2015, 2020; Roger et al., 2020; Benmammar et al., 2020; Štípská & Powell, 2005).

Bulk rock compositions indicate that the protolith of Lac Cornu eclogite has a geochemical signature of tholeiitic basalt, probably N-type MORB (Fig. S1; this study; Paquette et al., 1989; Liégeois & Duchesne, 1981), as also reported for amphibolites near the Emosson Lake (von Raumer et al., 1990). The U/Pb zircon ages at 461.6 ± 1.2 Ma and 461.7 ± 1.6 Ma (Fig. 13) were obtained on euhedral zircons or inherited cores that show oscillatory zoning (Fig. 12) and high Th/U ratios (>0.1) typical of magmatic zircon (Teipel et al., 2004; Linnemann et al., 2011). Thus, these ages are interpreted as the emplacement age of the tholeiitic protolith, in agreement with previous studies in the ARM (Paquette et al., 1989; Bussy et al., 2011), in the Argentera, Belledonne and Pelvoux massifs (Paquette et al., 1989; Rubatto et al., 2001, 2010; Fréville, 2016) (Table 1). Moreover, these zircons are enriched in HREEs over MREEs and have a positive Ce anomaly and negative Eu anomaly (Fig. 14), indicating a crystallization in the presence of plagioclase (Rubatto, 2002; Hoskin & Schaltergger; 2003). Thus, trace and REE patterns suggest that the eclogite protoliths from the ARM, Belledonne and Argentera massifs were tholeiitic sills or dykes intruding a thinned continental crust (Paquette et al., 1989; Ménot & Paquette, 1993; Rubatto et al., 2010). This interpretation is consistent with Ordovician magmatism observed in the whole northern Gondwana margin (e.g. Melleton et al., 2010 and references therein). Recently, Jouffray et al. (2020) identified a crustal-contamination in the geochemical signature of the basaltic protolith of the Argentera massif eclogite that could indicate high-temperature hydrothermal alteration or formation in a supra-subduction zone context. Unlike the late Devonian eclogites of the internal zone of the Variscan belt (e.g. Paquette et al., 2017), the ARM eclogites are not associated with blueschist facies metamorphic units as expected in a subduction process and do not record the typical low-temperature gradient of subduction zone (e.g. Ernst, 1971). Moreover, our thermodynamic models indicate that the mafic rocks were not H_2O-saturated (Fig. S2A and B) as expected for subducted oceanic crust (e.g. Katayama et al., 2003; Faccenda et al., 2009; Angiboust and Agard, 2010; van Keken et al., 2011; Freundt et al., 2014). Therefore, we suggest that burial and eclogite metamorphism of basaltic protolith are the result of continental crust thickening as proposed in some recent studies in the ECMs and the Montagne Noire (Jacob et al., 2021; Whitney et al., 2015, 2020; Roger et al., 2020).

5.3. Comparison with other eclogites from the South-Western branch of the Variscan belt

Our *P–T* results of 1.75 GPa at 710 °C are slightly higher in pressure than those documented in previous studies in the ARM (Fig. 15; Table 1). Compared to other ECMs, the peak pressure conditions of HP metamorphism in the ARM are similar to the ~1.8 GPa recorded in the Gothard massif (Abrecht et al., 1991; Biino, 1994), but slightly higher than the ~1.5 GPa estimated in the Argentera massif (Ferrando et al., 2008; Jouffray et al., 2020) or the 1.4 GPa estimated in the NE Belledonne massif (Jacob et al., 2021) (Fig. 15B). Our *P–T* path of the ARM is similar to those calculated for the eclogites from the Montagne Noire gneiss dome (Whitney et al., 2015, 2020; Pitra et al., 2021) and the Sardinia-Corsica massifs (Giacomini et al., 2005; Libourel & Vielzeuf, 1988; Cortesogno et al., 2004; Cruciani et al., 2011, 2012, 2015, 2021) (Fig. 15B), and also for pre-alpine eclogites occurrences in the internal Alps in the Adula, Tambo and Suretta nappes (see Biino et al., 1997).

Regarding our U-Pb age of the HP metamorphic stage (*c.* 330–340 Ma), similar ages were also determined on zircon and rutile formed under HP conditions in the Argentera massif (Rubatto et al., 2001, 2010) and in the Belledonne massif (Jacob et al., 2021) (Table 1). These results are also consistent with the timing of HP prograde metamorphism in the Maures-Tanneron massif that ended at *c.* 331 Ma (monazite EPMA, Oliot et al., 2015). The timing of the HP in the Montagne Noire massif is still debated: *c.* 315 Ma estimated by U-Pb on zircon (Whitney et al., 2015, 2020) or *c*. 360 Ma estimated by Sm-Nd on garnet and U-Pb on zircon (Pitra et al., 2021; Faure et al., 2014).

Given the *P–T* conditions, the shape of the *P–T* path and the geochronological record, the eclogites of the ARM can be compared with those of the Belledonne, Argentera and Sardinia-Corsica massifs that share a similar timing and *P–T* evolution (Fig. 15) with peak pressure conditions between 1.5–2 GPa at 600–750 °C (Fig.14; Table 1) (Cruciani et al., 2011, 2012, 2015, 2021; Giacomini et al., 2005; Franceschelli et al., 2007; Ferrando et al., 2008; Jouffray et al., 2020; Jacob et al., 2021). The *P–T–t* similarities between eclogites of the ARM and others massifs of the south-western branch of the Variscan belt suggest that all these mafic rocks might be the HP relics of the root of an orogenic plateau that could correspond to the French Central massif (Vanderhaeghe et al., 2020).

Interestingly, in all the aforementioned massifs, the eclogitic rocks crop out in or near kilometre-wide wrenching continental shear zone corridors. In the Montagne Noire massif, an intracontinental thickening along a kilometre-wide transpressional shear zone is proposed to explain the burial and eclogitization (Whitney et al., 2020). A similar system can be invoked for the burial of the deep crust, in addition to the nappe stacking that was previously documented in the in the ARM (Dobmeier, 1998; von Raumer & Bussy, 2004) and dated at *c.* 340 Ma in the adjacent Belledonne massif (e.g. Fréville et al., 2018).

5.4. Exhumation of the eclogites

In the south-western branch of the Variscan belt, the presence of HP rocks is often associated with vertical transcurrent shear zones (*Sardinia-Corsica*: Giacomini et al., 2008; Cruciani et al., 2011, 2012, 2015; *Montagne Noire*: Whitney et al., 2015, 2020; Trap et al., 2017; Roger et al., 2020; *External Crystalline massifs*: Jouffray et al., 2020; this study; *Maures-Tanneron*: Schneider et al., 2014) (Fig. 1). In these different domains, the exhumation of eclogite-bearing deep crust is mainly explained by vertical-upwelling dominated processes, assisted by vertical channel flow (Rey et al., 2011, 2017; Whitney et al., 2015, 2020), diapirism (Faure et al., 2014; Soula et al., 2001; Charles et al., 2009) and /or vertical extrusion during transpression (Schneider et al., 2014; Gerbault et al., 2018; Simonetti et al., 2020b). Nonetheless, mineral and stretching lineations in the vertical planar foliations in the ARM are mainly gently dipping, in agreement with dominant strike-slip motion but in apparent disagreement with a direct vertical motion (e.g. von Raumer & Bussy, 2004; Simonetti et al., 2020a).

In the Montagne Noire Massif, occurrences of HP mafic are described within and at the periphery of a dextral continental scale transcurrent shear zone associated with a double migmatitic dome structure (e.g. Rabin et al., 2015; Whitney et al, 2015, 2020; Roger et al., 2020). Several authors proposed that these eclogites were rapidly exhumed through a vertical channel flow from 1.5 GPa to 0.5 GPa within a few million years from the deep orogenic crust setting (Rey et al., 2011, 2017; Whitney et al., 2015, 2020). This model is supported by a short time gap of less than 5 Ma between the age of HP metamorphism and widespread partial melting occurring at lower pressure in the Montagne Noire Massif (Whitney et al., 2015, 2020; Roger et al., 2015, 2020; Trap et al., 2017). Recorded exhumation was much slower in the ARM and lasted c. 35 Ma from c. 335 Ma to 300 Ma, suggesting a different integrated-time exhumation mechanism.

The decompression history, from 1.75 to 1.0 GPa (Fig. 15) is recorded in symplectites of the core of eclogitic lenses where the flat-lying S_H is observed. These results support the idea that the first stage of exhumation was accommodated by horizontal flow that is widely documented in mature orogenic plateau (e.g. Beaumont et al., 2001; Vanderhaeghe, 2009; Rosenberg et al., 2007) and may induce significant unroofing if the flow is not strictly horizontal (e.g. Trap et al., 2011). Such horizontal flow is described in the French Central massif (Vanderhaeghe et al., 2020; Roger et al., 2020) and in the Bohemian massif (e.g. Schulmann et al., 2005, 2008).

The second stage of the exhumation path is recorded within amphibolitic facies of metabasites and corresponds to the vertical dextral transpression and related planar surface S_V (Fig. 15). Dextral shear zones show a stretching lineation that plunges at c. 35° toward the north mainly and sometimes more (von Raumer & Bussy, 2004). Consequently, a horizontal displacement of 50-60 km is sufficient to account for a vertical exhumation of about 30 km. Such horizontal displacement is far below the 300 km offset considered for the External Variscan Shear Zone ("ECM SZ" in Guillot et al., 2009). Furthermore, our thermodynamic models indicate an increase in the water content during the exhumation. This is consistent with the aqueous fluid drainage reported in the dextral shear zones of the ARM (Genier et al., 2008), and further argues for the role of transpressional shearing during the exhumation of eclogites. Exhumation of partially molten crust along crustal scale transpressive shear zone is well documented in the Variscan belt (Pereira et al., 2017). One may consider that the buoyancy-driven vertical flow might have also partly contributed to the exhumation of the eclogite bearing partially-molten crust. These results suggest that exhumation of the HP–HT eclogites in the SE branch of the Variscan belt was mostly accommodated by horizontal flow along transpressional shear zones, as proposed in the Sardinia massif (Giacomini et al., 2008; Cruciani et al., 2011; Carosi et al., 2009), in the Maures-Tanneron massif (Corsini & Rolland, 2009) or in the Central Iberian Zone (Pereira et al., 2017).

6. Conclusion

Geochemical, petrological and thermodynamic modelling associated to U-Th-Pb geochronology, structural and microstructural analyses permitted to reconstruct the *P–T–t–D* path of the Lac Cornu eclogites in the ARM. Our results obtained on weakly and strongly retrogressed eclogites highlight the following tectono-metamorphic evolution: (i) emplacement of a tholeiitic protolith at *c.* 461 Ma; (ii) a high-pressure stage (M1) at 710°C and 1.75 GPa dated at *c.* 340–330 Ma; (iii) a first decompression stage (M2) down to pressures around 1.0 GPa at temperatures between 650 °C and 775 °C during a horizontal flow of the partially-molten lower crust followed by (iv) final unroofing below 0.5 GPa and 500 °C (M3) mainly accommodated by dextral transpressive deformation. Cooling at low pressure conditions ended at *c.* 300 Ma. Based on these results and a comparison with the others surrounding Variscan massifs, we propose that the eclogites of the ECMs correspond to exhumed portions of root of orogenic thickened crust of the Variscan belt after the collision of the Galatian-Armorica terranes.

Acknowledgements

This work was supported by the BRGM through the Référentiel Géologique de la France program (RGF program). We thank two anonymous reviewers and Simon Harley for his constructive and helpful comments as well as the editorial handling of this manuscript. We thank Cyprien Astoury for mineral separation, Didier Convert-Gaubier for his generous support with thin section preparation–and Jean-Luc Devidal for his help during REE analyses acquisition. The newly acquired and compiled structural data will be available on the RGF website (http://rgf.brgm.fr).

References

Abrecht, J., Biino, G. G., Mercolli, I., & Stille, P. (1991). Mafic-ultramafic rock associations in the Aar, Gotthard and Tavetsch massifs of the Helvetic domain in the Central Swiss Alps: markers of ophiolitic pre-Variscan sutures, reworked by polymetamorphic events? *Schweizerische Mineralogische und Petrographische Mitteilungen*, 71, 295–300.

Aleinikoff, J. N., Wintsch, R. P., Fanning, C. M., & Dorais, M. J. (2002). U-Pb geochronology of zircon and polygenetic titanite from the Glastonbury Complex, Connecticut, USA: An integrated SEM, EMPA, TIMS, and SHRIMP study. *Chemical Geology*, 188, 125–147, doi:10.1016/S0009-2541(02)00076-1.

Angiboust, S., Agard, P. (2010). Initial water budget: the key to detaching large volumesof eclogitized oceanic crust along the subduction channel? *Lithos* 120, 453–474.

Ballèvre, M., Manzotti, P., & Dal Piaz, G. V. (2018). Pre-Alpine (Variscan) inheritance: A key for the location of the future Valaisan Basin (Western Alps). *Tectonics*, 37, 786–817.

Beaumont, C., Jamieson, R.A., Nguyen, M.H., Lee, B. (2001). Himalayan tectonics explained by extrusion of a low-viscosity crustal channel coupled to focused surface denudation. *Nature,* 414, 738–742.

Bellahsen, N., Mouthereau, F., Boutoux, A., Bellanger, M., Lacombe, O., Jolivet, L., & Rolland, Y. (2014). Collision Kinematics in the Western External Alps. *Tectonics,* 33. https://doi.org/10.1002/2013TC003453.

Bellanger, M., Bellahsen, N., Jolivet, L., Baudin, T., Augier, R., & Boutoux, A. (2014). Basement shear zones development and shortening kinematics in the Ecrins Massif, Western Alps. *Tectonics*, 33, 84–111.

Bellière, J. (1958). Contribution à l'étude pétrogénétique des schistes cristallins du massif des Aiguilles Rouges. *Annales de la Société géologique de Belgique,* 81, 1–198.

Bellot, J.-P., Laverne, C. & Bronner, G. (2010). An early Palaeozoic supra-subduction lithosphere in the Variscides: new evidence from the Maures massif. *International Journal of Earth Sciences*, 99, 473–504.

Benmammar, A., Berger, J., Triantafyllou, A., Duchene, S., Bendaoud, A., Baele, J.M., … Diot, H. (2020). Pressure-temperature conditions and significance of Upper Devonian eclogite and amphibolite facies metamorphisms in southern French Massif central. *Bulletin de la Société géologique de France*, 191. doi.org/10.1051/bsgf/2020033

Berger, J., Féménias, O., Ohnenstetter, D., Bruguier, O., Plissart, G., Mercier, J.-C.C., Demaiffe, D. (2010). New occurrence of UHP eclogites in Limousin (French Massif Central): age, tectonic setting and fluid-rock interactions. *Lithos*, 118, 365–382.

Biino, G. G. (1994). The pre-Late Ordovician metamorphic evolution of the Gotthard-Tavetsch massifs (Central Alps): From lawsonite to kyanite eclogites to granulite retrogression. *Schweizerische Mineralogische und Petrographische Mitteilungen*, 74, 87–104.

Biino, G. G., & Meisel, T. (1993). Geochemistry of Polymetamorphic Ultramafics (Major, Trace, Noble and Rare Earth Elements): an Example From the Helvetic Basement, Central Alps, Switzerland. *Mineralogy and Petrology*, 49, 189-212.

Biino, G., Marquer, D., Nussbaum, C. (1997). Alpine and Pre-Alpine subduction events in polycyclic basements of the Swiss Alps. *Geology*, 25 (8), 751–754.

Boutoux, A., Bellahsen, N., Nanni, U., Pik, R., Verlaguet, A., Rolland, Y., & Lacombe, O. (2016). Thermal and Structural Evolution of the External Western Alps: Insights from (U–Th–Sm)/He Thermochronology and RSCM Thermometry in the Aiguilles Rouges/Mont Blanc Massifs. *Tectonophysics*, 683, 109-23. https://doi.org/10.1016/j.tecto.2016.06.010.

Bracciali, L., Parrish, R.R., Horstwood, M.S.A., Condon, D.J., & Najman, Y. (2013). U-Pb LA-(MC)-ICP-MS dating of rutile: New reference materials and applications to sedimentary provenance. *Chemical Geology*, 347, 82-101.

Bussy, F., von Raumer, J.F. (1993). U–Pb dating of Paleozoic events in the Mont-Blanc crystalline massif, Western Alps. *Terra Nova*, 5, 382.

Bussy, F., & von Raumer, J.F. (1994). U–Pb geochronology of Palaeozoic magmatic events in the Mont-Blanc Crystalline Massif,Western Alps. *Schweizerische Mineralogische und Petrographische Mitteilungen*, 74, 514–515.

Bussy, F., Hernandez, J., & von Raumer, J.F. (2000). Bimodal magmatism as a consequence of the post-collisional re-adjustment of the thickened Variscan continental lithosphere (Aiguilles Rouges/Mont-Blanc Massifs, western Alps). *Transactions of the Royal Society of Edinburgh–Earth Sciences*, 91, 221–233.

Bussy, F., Péronnet, V., Ulianov, A., Epard, J.L., & von Raumer, J. (2011). Ordovician magmatism in the External French Alps: witness of a peri-Gondwanan active continental margin. In Gutiérrez-Marco, J.C., Rábano, I., & García-Bellido, D., eds., The Ordovician of the World: Madrid, Instituto Geológico y Minero de España, Cuadernos del Museo Geominero, v. 14, p. 75–82.

Capuzzo, N., Handler, R., Neubauer, F., & Wetzel, A. (2003). Post-collisional rapid exhumation and erosion during continental sedimentation: The example of the late-Variscan Salvan-Dorenaz basin (western Alps). *International Journal of Earth Sciences*, 92, 364–379. doi:10.1007/s00531-003-0332-0.

Carreras, J., & Druguet, E. (2014). Framing the tectonic regime of the NE Iberian Variscan segment. *Geological Society Special Publication London* 405. doi.org/10.1144/SP405.7

Carosi, R., Frassi, C., & Montomoli, C. (2009). Deformation during exhumation of medium- and high-grade metamorphic rocks in the Variscan chain in northern Sardinia (Italy). *Geological Journal* 44, 280–305.

Charles, N., Faure, M., & Chen, Y. (2009). The Montagne Noire migmatite dome emplacement (French Massif Central): New insights from petro fabric and AMS studies. *Journal of Structural Geology*, 31, 1423–1440. doi:10.1016/j.jsg.2009.08.007.

Chiaradia, M. (2003). Formation and Evolution Processes of the Salanfe W–Au–As-Skarns (Aiguilles Rouges Massif, Western Swiss Alps). *Mineralium Deposita*, 38, 154-68. https://doi.org/10.1007/s00126-002-0296-1.

Chopin, C. (1984). Coesite and pure pyrope in high-grade blueschists of the western Alps: a first record and some consequence. *Contribution to Mineralogy and Petrology*, 86, 107–118.

Connolly, J.A.D. (2005). Computation of phase equilibria by linear programming: a tool for geodynamic modeling and its application to subduction zone decarbonation. *Earth Planetary Science Letters*, 236, 524–541.

Corfu, F., Hanchar, J. M., Hoskin, P. W. O., & Kinny, P. (2003). Atlas of zircon textures. In: Hanchar, J. M. & Hoskin, P. W. O. (eds) Zircon. *Mineralogical Society of America, Reviews in Mineralogy and Geochemistry*, 53, 469-500.

Corsini, M., & Rolland, Y. (2009). Late evolution of the southern European Variscan belt: exhumation of the lower crust in a context of oblique convergence. *Comptes Rendus Geosciences*, 341, 214–223.

Cortesogno, L., Gaggero, L., Oggiano, G., & Paquette, J. L. (2004). Different tectono-thermal evolutionary paths in eclogitic rocks from the axial zone of the Variscan chain in Sardinia (Italy) compared with the Ligurian Alps. *Ofioliti*, 29, 125–144.

Cruciani, G., Franceschelli, M., & Groppo, C. (2011). P–T evolution of eclogite-facies metabasite from NE Sardinia, Italy: insights into the prograde evolution of Variscan eclogites. *Lithos,* 121(1), 135–150.

Cruciani, G., Franceschelli, M., Groppo, C., & Spano, M. E. (2012). Metamorphic evolution of non-equilibrated granulitized eclogite from Punta de li Tulchi (Variscan Sardinia) determined through texturally controlled thermodynamic modelling. *Journal of Metamorphic Geology*, 30, 667–685.

Cruciani, G., Franceschelli, M., Langone, A., Puxeddu, M., & Scodina, M. (2015). Nature and age of pre-Variscan eclogite protoliths from the Low-to Medium-Grade Metamorphic Complex of north–central Sardinia (Italy) and comparisons with coeval Sardinian eclogites in the northern Gondwana context. *Journal of Geological Society*, 172(6), 792–807.

Cruciani, G., Franceschelli, M., Massonne, H.J., Musumeci, G. (2021). Evidence of two metamorphic cycles preserved in garnet from felsic granulite in the southern Variscan belt of Corsica, France. *Lithos*, 380–381, 105919.

Dobmeier, C. (1998). Variscan P-T deformation paths from the southwestern Aiguilles Rouges Massif (External massif, western Alps) and their implication for its tectonic evolution. *Geologische Rundschau*, 87, 107–123, doi:10.1007/s005310050193.

Duesterhoeft, E., & Lanari, P. (2020). Iterative thermodynamic modelling—Part 1: A theoretical scoring technique and a computer program (Bingo-Antidote). *Journal of Metamorphic Geology*, 8, 527–551.

Duchene, S., Lardeaux, J.M., & Albarède, F. (1997). Exhumation of eclogites: insights from depth–time path analysis. *Tectonophysics* 280 (1–2), 125–140.

Faccenda, M., T. V. Gerya, and L. Burlini (2009), Deep slab hydration induced by bending-related variations in tectonic pressure, Nature Geosciences, 2, 790–793.

Faure, M., & Cottereau, N. (1988). Données cinématiques sur la mise en place du dôme migmatitique carbonifère moyen de la zone axiale de la Montagne Noire (Massif Central, France). *Comptes Rendus Académiques scientifiques de Paris*, 307, 1787–1794.

Faure, M., Cocherie, A., Gaché, J., Esnault, C., Guerrot, C., Rossi, P., … Qiuli, L. (2014). Middle Carboniferous intracontinental subduction in the Outer Zone of the Variscan Belt (Montagne Noire Axial Zone, French Massif Central): multi-method geochronological approach of polyphase metamorphism. In: Schulmann, K., Martinez Catalan, J.R., Lardeaux, J.M., Janousek, V., Oggiano, G. (Eds.), The Variscan Orogeny: Extent, Timescale and the Formation of the European Crust. *Geological Society of London, Special Publication*, 405. http://dx.doi.org/10.1144/SP405.2.

Ferrando, S., Lombardo, B., & Compagnoni, R. (2008). Metamorphic history of HP mafic granulites from the Gesso-Stura Terrain (ArgenteraMassif, Western Alps, Italy). *European Journal of Mineralogy*, 20, 777–790.

Franceschelli, M., Puxeddu, M., Cruciani, G. & Utzeri, D. (2007). Metabasites with eclogite facies relics from Variscides in Sardinia, Italy: a review. *International Journal of Earth Sciences*, 96, 795–815.

Franke, W., Cocks, L. R. M., & Torsvik, T. H. (2017). The Palaeozoic Variscan oceans revisited. *Gondwana Research*, 48, 257-284.

Freundt, A., Grevemeyer, I., Rabbel, W., Hansteen, T.H., Hensen, C., Wehrmann, H., … Frische, M. (2014). Volatile (H2O, CO2, Cl, S) budget of the Central American subduction zone. *International Journal of Earth Science*, 103, 2101–2127.

Fréville, K. (2016). The variscan orogeny in the external crystalline massifs of Belledonne and Pelvoux (French Western Alps): the role of partial melting and plutonism on the structuration of the continental crust, (Doctoral dissertation). Retrieved from HAL (https://tel.archives-ouvertes.fr/tel-01968058/). Orléans, France, Université de Orléans.

Freville, K., Trap, P., Faure, M., Melleton, J., Li, X.H., Lin, W., Blein, O., Bruguier, O., Poujol, M. (2018). Structural, metamorphic and geochronological insights on the Variscan evolution of the Alpine basement in the Belledonne Massif (France). *Tectonophysics*, 726, 14–42.

Frost, B.R., Chamberlain, K.R., & Schumacher, J.C. (2000). Sphene(titanite): phase relations and role as a geochronometer. *Chemical Geology*, 172, 131–148.

Fuhrman, M. L., & Lindsley, D. H. (1988). Ternary-feldspar modeling and thermometry. *American Mineralogist*, 73, 201–215.

Genier, F., Bussy, F., Epard, J.L, & Baumgartner, L. (2008). Water-Assisted Migmatization of Metagraywackes in a Variscan Shear Zone, Aiguilles-Rouges Massif, Western Alps. *Lithos*, 102, 575-97. https://doi.org/10.1016/j.lithos.2007.07.024.

Gerbault, M., Schneider, J., Reverso-Peila, A., & Corsini, M. (2018). Crustal exhumation during ongoing compression in the Variscan Maures-Tanneron Massif, France - geological and thermo-mechanical aspects. *Tectonophysics*, 746, 439–458.

Getsinger, A.J., & Hirth, G. (2014). Amphibole fabric formation during diffusion creep and the rheology of shear zones. *Geology*, 42, 535–538. doi:10.1130/G35327.1

Giacomini, F., Bomparola, R.M., & Ghezzo, C. (2005). Petrology and geochronology of metabasites with eclogite facies relics from NE Sardinia: constraints for the Palaeozoic evolution of Southern Europe. *Lithos*, 82(1), 221–248.

Giacomini, F., Braga, R., Tiepolo, M., Tribuzio, R. (2007). New constraints on the origin and age of Variscan eclogitic rocks (Ligurian Alps, Italy). *Contribution to Mineralogy and Petrology*, 153(1), 29–53.

Giacomini, F., Dallai, L., Carminati, E., Tiepolo, M., & Ghezzo, C. (2008). Exhumation of a Variscan orogenic complex: insights into the composite granulitic–amphibolitic metamorphic basement of south-east Corsica (France). *Journal of Metamorphic Geology*, 26, 403–436.

Green, E. C. R., Holland, T. J. B. & Powell, R. (2007). An order-disorder model for omphacitic pyroxenes in the system jadeite-diopside-hedenbergite-acmite, with applications to eclogitic rocks. *American Mineralogist*, 92, 1181–1189.

Green, E.C.R., White, R.W., Diener, J.F.A., Powell, R., Holland, T.J.B. & Palin, R.M. (2016). Activity–composition relations for the calculation of partial melting equilibria in metabasic rocks. *Journal of Metamorphic Geology*, 34, 845–869.

Guillot, S., & Ménot, R.P. (2009). Paleozoic evolution of the External Crystalline Massifs of the Western Alps. *Comptes Rendus Geosciences*, 341(2-3), 253-265. https://doi.org/10.1016/j.crte.2008.11.010

Guillot, S., di Paola, S., Ménot, R.P., Ledru, P., Spalla, M., Gosso, G., & Schwartz, S. (2009). Suture zones and importance of strike-slip faulting for Variscan geodynamic reconstructions of the external crystalline massifs of the Western Alps. *Bulletin de la Société géologique de France*, 180, 483–500.

Holland, T., & Blundy, J. (1994) Non-ideal interactions in calcic amphiboles and their bearing on amphibole-plagioclase thermometry. *Contributions to Mineralogy and Petrology*, 116, 433–447. doi:10.1007/BF00310910.

Holland, T.J.B., & Powell, R. (2011). An improved and extended internally consistent thermodynamic dataset for phases of petrological interest, involving a new equation of state for solids. *Journal of Metamorphic Geology*, 29, 333–383.

Hoskin, P.W.O., & Schaltergger, U. (2003). The composition of zircon and igneous and metamorphic petrogenesis. *Review of Mineral Geochemistry,* 53, 27–62.

Hurai, V., Paquette, J.L., Huraiová, M., & Konečný, P. (2010). Age of deep crustal magmatic chambers in the intra-Carpathian back-arc basin inferred from LA-ICPMS U-Th-Pb dating of zircon and monazite from igneous xenoliths in alkali basalts. *Journal of Volcanology and Geothermal Research*, 198, 275-287.

Irvine, T.N., Barragar, W.R.A. (1971). A guide to the chemical classification of the common volcanic rocks. *Canadian Journal of Earth Sciences*, 8, 523–548.

Jackson, S.E., Pearson, N.J., Griffin, W.L., & Belousova, E.A. (2004). The application of laser ablation-inductively coupled plasma-mass spectrometry to in situ U–Pb zircon geochronology. *Chemical Geology*, 211, 47-69.

Jacob, J-B., Guillot, S., Rubatto, D., Janots, E., Melleton, J., & Faure, M. (2021). Carboniferous high-pressure metamorphism and deformation in the Belledonne Massif (Western Alps). *Journal of Metamorphic Geology,* doi:10.1111/jmg.12600.

Jaffey, A.H., Flynn, K.F., Glendenin, L.E., Bentley, W.C., & Essling, A.M. (1971). Precision measurement of half-lives and specific activities of 235U and 238U. *Physical Review C,* 4, 1889-1906.

Jouffray, F., Spalla, M.I., Lardeaux, J.M., Filippi, M., Rebay, G., Corsini, M., … Gosso, G. (2020). Variscan eclogites from the Argentera-Mercantour Massif (External Crystalline Massifs, SW Alps): a dismembered cryptic suture zone. *International Journal of Earth Sciences*, 109, 1273–1294. https://doi.org/10.1007/s00531-020-01848-2.

Joye, J.B. (1989). L'évolution pression-température-déformation dans le massif des Aiguilles Rouges, massif externe alpin, (Doctoral dissertation). Retrieved from HAL (https://tel.archives-ouvertes.fr/tel-00822947/). Fribourg, Switzerland, Université de Fribourg.

Kim, J. & Jung, H. (2019). New crystal preferred orientation of amphibole experimentally found in simple shear. *Geophysical Research Letters*, 46, 12996–13005. https://doi.org/10.1029/2019GL085189

Ko, B., & Jung, H. (2015). Crystal preferred orientation of an amphibole experimentally deformed by simple shear. *Nature Communication*, 6, doi:10.1038/ncomms7586.

Konzett, J., Rhede, D., & Frost, D.J. (2012) The high-PT stability of apatite and Cl partitioning between apatite and hydrous potassic phases in peridotite: An experimental study to 19 GPa with implications for the transport of P, Cl and K in the upper mantle. *Contributions to Mineralogy and Petrology*, 163, 277–296. doi: 10.1007/s00410-011-0672-x.

Kroner, A., & Romer, R.L. (2013). Two plates – many subduction zones: the Variscan orogeny reconsidered. *Gondwana Research*, 24(1), 298–329.

Krummenacher, D. (1959). Le cristallin de la région de Fully (Valais). *Schweizerische Mineralogische und Petrographische Mitteilungen*, 39, 151-266.

Lanari, P., Riel, N., Guillot, S., Vidal, O., Schwartz, S., Pêcher, A., Hattori, K.H. (2013). Deciphering high-pressure metamorphism in collisional context using microprobe mapping methods: application to the Stak eclogitic massif (northwest Himalaya). *Geology,* 41(2), 111–114. https://doi.org/10.1130/g33523.1.

Lanari, P., Vidal, O., de Andrade, V., Dubacq, B., Lewin, E., Grosch, E., & Schwartz, S. (2014). XMapTools: a MATLAB-based program for electron microprobe X-ray image processing and geothermobarometry. *Computers & Geosciences*, 62, 227–240.

Lanari, P., & Engi, M. (2017). Local bulk composition effects on metamorphic mineral assemblages. *Reviews in Mineralogy and Geochemistry*, 83, 55–102.

Lanari, P., Vho, A., Bovay, T., Airaghi, L., & Centrella, S., (2019). Quantitative compositional mapping of mineral phases by electron probe micro-analyser. *Geological Society of London, Special Publications*, 478, 39-63.

Lardeaux, J.M., Ledru, P., Daniel, I., Duchene, S. (2001). The Variscan French Massif Central – a new addition to the ultra-high pressure metamorphic 'club': exhumation processes and geodynamic consequences. *Tectonophysics*, 332, 143–167.

Latouche, L., & Bogdanoff, S. (1987). Evolution précoce du massif de l'Argentera: Apport des éclogites et des granulites. *Géologie Alpine*, 63,151–164.

Laurent, O., Couzinié, S., Zeh, A., Vanderhaeghe, O., Moyen, J.F., Villaros, A., … & Chelle-Michou, C. (2017). Protracted, coeval crust and mantle melting during Variscan late-orogenic evolution: U–Pb dating in the eastern French Massif Central. *International Journal of Earth Sciences*, 106, 421-451.

Leake, B.E., Woolley, A.R., Arps, C.E.S., Birch, W.D., Gilbert, M.C., Grice, J.D., … Youzhi, G. (1997). Nomenclature of amphiboles: report of the subcommittee on amphiboles of the International Mineralogical Association Commission on New Minerals and Mineral Names. *Mineral Magazine,* 61, 295–321.

Le Bas, M.J., Le Maitre, R.W., Streckeisen, A., & Zanettin, B. (1986). A chemical classification of volcanic rocks based on the total alkali-silica diagram. *Journal of Petrology*, 27, 445-450.

Libourel, G., & Vielzeuf, D. (1988). Isobaric cooling at high pressure: the example of Corsican high pressure granulites. *Terra Cognita,* 8, 268.

Liégeois, J.-P., & Duchesne, J.-C. (1981). The Lac Cornu retrograded eclogites (Aiguilles Rouges massif, Western Alps, France): Evidence of crustal origin and metasomatic alteration. *Lithos*, 14, 35–48.

Linnemann, U., Ouzegane, K., Drareni, A., Hofmann, M., Becker, S., Gärtner, A., & Sagawe, A. (2011). Sands of West Gondwana: anarchive of secular magmatism and plate interactions - a case study from the Cambro-Ordovician section of the Tassili Ouan Ahaggar (Algerian Sahara) using U–Pb LA-ICP-MS detrital zircon ages. *Lithos,* 123, 188–203.

Lotout, C., Pitra, P., Poujol, M., Anczkiewicz, R., & Van Den Driessche, J. (2018). Timing and duration of Variscan high-pressure metamorphism in the French Massif central: a multimethod geochronological study from the Najac Massif. *Lithos,* 308–309, 381–394.

Lotout, C., Poujol, M., Pitra, P., Anczkiewicz, R., & Van Den Driessche, J. (2020). From Burial to Exhumation: Emplacement and Metamorphism of Mafic Eclogitic Terranes Constrained Through Multimethod Petrochronology, Case

Study from the Lévézou Massif (French Massif Central, Variscan Belt). *Journal of Petrology*, doi: 10.1093/petrology/egaa046

Ludwig, K.R., 2001. User manual for Isoplot/Ex rev. 2.49. A geochronological toolkit for Microsoft Excel. *Berkeley Geochronology Center Special Publication*, 1a, 1–56.

Maierová P, Schulmann K, Lexa O et al. 2016. European Variscan orogenic evolution as ananalogue of Tibetan-Himalayan orogen: Insights from petrology and numerical modeling. Tectonics 35:1760–1780.

Matte, P. (1991). Accretionary history and crustal evolution of the Variscan Belt in western Europe. *Tectonophysics*, 196, 309–337.

Matte, P. (1998). Continental subduction and exhumation of HP rocks, in Paleozoic orogenic belts: Uralides and Variscides. GFF, Vol. 120 (Pt. 2, June), pp. 209–222. Stockholm. ISSN 1103-5897.

Melleton, J., Cocherie, A., Faure, M., Rossi, P. (2010). Precambrian protoliths and Early Paleozoic magmatism in the French Massif Central: U–Pb data and the North Gondwana connection in the west European Variscan belt. *Gondwana Research*, 17, 13–25.

Ménot, R.-P., & Paquette, J.-L. (1993). Geodynamic significance of basic and bimodal magmatism, in the External domain. in von Raumer, J.F., and Neubauer, F., eds., The Pre-Mesozoic Geology in the Alps: Heidelberg, Germany, Springer-Verlag, p. 241–254.

Meschede, M. (1986). A method of discriminating between different types of mid-ocean ridge basalts and continental tholeiites with the Nb–Zr–Y diagram. *Chemical Geology*, 56, 207–218.

Miller, C., & Thöni, M. (1995). Origin of eclogites from the Austro-alpine basement (Tirol, Austria): geochemistry and Sm–Nd vs. Rb–Sr isotope systematics. *Chemical Geology*, 122, 199–225.

Müller, W., Shelley, M., Miller, P. & Broude, S. (2009). Initial performance metrics of a new custom-designed ArF excimer LA-ICPMS system coupled to a two-volume laser-ablation cell. *Journal of Analytical Atomic Spectrometry*, 24, 209-214.

O'Brien, P.J. (1997). Garnet zoning and reaction textures in overprinted eclogites, Bohemian Massif, European Variscides: a record of their thermal history during exhumation. *Lithos* 41,119–133.

O'Brien, P.J., Zotov, N., Law, R., Khan, M.A., Jan, & M.Q. (2001). Coesite in Himalayan eclogite and implications for models of India–Asia collision. *Geology*, 29, 435–438.

Oberli, F., Meier, M., & Biino, G. G. (1994). Time constraints on the pre-Variscan magmatic/metamorphic evolution of the Gotthard and Tavetsch units derived from U-Pb results. *Schweizerische Mineralogische und Petrographische Mitteilungen*, 74, 483–488.

Oliot, E., Melleton, J., Schneider, J., Corsini, M., Gardien, V., Rolland, Y. (2015). Variscan crustal thickening in the Maures-Tanneron massif (South Variscan belt, France): new in situ monazite U-Th-Pb chemical dating of high-grade rocks. *Bulletin de la Société géologique de France*, 186, 145–169.

Papapavlou, K., Darling, J.R., Storey, C.D., Lightfoot, P.C., Moser, D.E., & Lasallea, S. (2017). Dating shear zones with plastically deformed titanite: New insights into the orogenic evolution of the Sudbury impact structure (Ontario, Canada). *Precambrian Research*, 291, 220–235.

Pape, J., Mezger, K., & Robyr, M. (2016). A systematic evaluation of the Zr-in-rutile thermometer in ultra-high temperature (UHT) rocks. *Contribution to Mineralogy and Petrology*, 171, 1–20.

Paquette, J.L., & Tiepolo, M. (2007). High resolution (5 µm) U-Th-Pb isotopes dating of monazite with excimer laser ablation (ELA)-ICPMS. *Chemical Geology*, 240, 222-237.

Paquette, L., Ménot, R.P., & Peucat, J.J. (1989). REE, Sm-Nd and U-Pb zircon study of eclogites from the Alpine External massifs (Western Alps): Evidence for crustal contamination. *Earth and Planetary Science Letters*, 96, 181–198.

Paquette, J.L., Piro, J.L., Devidal, J.L., Bosse, V., & Didier, A. (2014). Sensitivity enhancement in LA-ICP-MS by N2 addition to carrier gas: application to radiometric dating of U–Th-bearing minerals. *Agilent ICP-MS Journal*, 58, 4–5.

Paquette, J.-L., Ballèvre, M., Peucat, J.-J., & Cornen, G. (2017). From opening to subduction of an oceanic domain constrained by LA-ICP-MSU–Pb zircon dating (Variscan belt, Southern Armorican Massif, France). *Lithos*, 294–295, 418–437.

Pearce, J.A. (1996). A user's guide to basalt discrimination diagrams. In: Wyman DA (ed) Trace element geochemistry of volcanic rocks: applications for massive sulphide exploration, vol 12. *Geological Association of Canada, Short Course Notes, Newfoundland*, pp 79–113.

Pereira, I., Dias, R., Bento dos Santos, T., & Mata, J. (2017). Exhumation of a migmatite complex along a transpressive shear zone: inferences from the Variscan Juzbado–Penalva do Castelo Shear Zone (Central Iberian Zone). *Journal of*

Geological Society of London, 174, 1004–1018. https://doi.org/10.1144/jgs2016-159

Pitra, P., Poujol, M., Van Den Driessche, J., Bretagne, E., Lotout, C., & Cogné, N. (2021). Late Variscan (315 Ma) subduction or deceiving zircon REE patterns and U-Pb dates from migmatite-hosted eclogites? (Montagne Noire, France). *Journal of Metamorphic Geology,* in press.

Rabin, M., Trap, P., Carry, N., Fréville, K., Cenki-Tok, B., Lobjoie, C., Goncalves, P., & Marquer, D. (2015). Strain partitioning along the anatectic front in the Variscan Montagne Noire massif (Southern French Massif Central). *Tectonics*, 34, 1709-1735. http://dx.doi.org/10.1002/2014TC003790

Regorda, A., Lardeaux, J.M., Roda, M.,Marotta, A. M., & Spalla, M. I. (2020). How many subductions in the Variscan orogeny? Insights from numerical models. *Geosciences Frontiers,* 11(3), 1025-1052.

Rey, P.F., Teyssier, C., Kruckenberg, S.C., & Whitney, D.L. (2011). Viscous collision in channel explains double domes in metamorphic core complexes. *Geology*, 39, 387–390.

Rey, P.F., Mondy, L., Duclaux, G., Teyssier, C., Whitney, D.L., Bocher, M., & Prigent, C. (2017). The origin of contractional structures in extensional gneiss domes. *Geology,* 45 (3), 263–266.

Roger, F., Teyssier, C., Respaut, J.-P., Rey, P.F., Jolivet, M., Whitney, D.L., Paquette, J.-L., & Brunel, M. (2015). Timing of formation and exhumation of the Montagne Noire double dome, French Massif Central. *Tectonophysics,* 640–641, 53–69. http://dx.doi.org/10.1016/j.tecto.2014.12.002.

Roger, F., Teyssier, C., Whitney, D.L., Respaut, J.P., Paquette, J.L., & Rey, P.F. (2020). Age of metamorphism and deformation in the Montagne Noire dome (French

Massif Central): Tapping into the memory of fine-grained gneisses using monazite U-Th-Pb geochronology. *Tectonophysics*, 776. doi.org/10.1016/j.tecto.2019.228316

Rolland, Y., Cox, S., Boullier, A.M., Pennacchioni, G., & Mancktelow, N. (2003). Rare earth and trace element mobility in mid-crustal shear zones: Insights from the Mont Blanc Massif (western Alps), *Earth Planetary Science Letters*, 214, 203–219.

Rosenberg, C. L., Medvedev, S., & Handy, M. R. (2007). Effects of Melting on faulting and Continental Deformation. *In* Handy, M. R., Hirth, G. & Hovious, N. (eds). Tectonic Faults, agents of change on a dynamic Earth: Report of the 95th Dahlem Workshop on the Dynamics of Fault Zones, Berlin, January 16-21, 2005.

Rossi, M., Rolland, Y., Vidal, O., & Cox, S. (2005). Geochemical variations and element transfer during shear zone development and related episyenites at middle crust depths: Insights from the Mont-Blanc granite (French-Italian Alps). In D. Brunh & L. Burlini (Eds.), High Strain Zones: Structure and Physical Properties, *Geological Society, London, Special Publication*, 245, 373-396. https://doi.org/10.1144/GSL.SP.2005.245.01.18

Rubatto, D. (2002). Zircon trace element geochemistry: distribution coefficients and the link between U–Pb ages and metamorphism. *Chemical Geology*, 184, 123–138.

Rubatto, D. (2017). Zircon: The metamorphic mineral. *Reviews in Mineralogy and Geochemistry*, 83, 261–295.

Rubatto, D., Ferrando, S., Compagnoni, R., & Lombardo, B. (2010). Carboniferous high-pressure metamorphism of Ordovician protolith in the Argentera Massif (Italy), Southern European Variscan Belt. *Lithos*, 116, 65–76.

Rubatto, D., Schaltegger, U., Lombardo, B., Colombo, F., & Compagnoni, R. (2001). Complex Paleozoic magmatic and metamorphic evolution in the Argentera Massif (Western Alps) resolved with U-Pb dating. *Schweizerische Mineralogische und Petrographische Mitteilungen*, 81, 213–228.

Schaltegger, U., Abrecht, J., Corfu, F. (2003). The Ordovician orogeny in the Alpine basement: constraints from geochronology and geochemistry in the Aar Massif (Central Alps). *Schweizerische mineralogische und petrographische Mitteilungen*, 83, 183-195.

Schneider, J., Corsini, M., Reverso, P.A., & Lardeaux, J.-M. (2014). Thermal and mechanical evolution of an orogenic wedge during Variscan collision: an example in the Maures-Tanneron Massif (SE France). *Geological Society of London*, *Special Publication*, 405, 313-331.

Schulmann, K., Kröner, A., Hegner, E., Wendt, I., Konopasek, J., Lexa, O., & Štípská, P. (2005) Chronological constraints on the pre-orogenic history, burial and exhumation of deep-seated rocks along the eastern margin of the Variscan orogen, Bohemian Massif, Czech Republic. *American Journal of Science* 305:407–448

Schulmann, K., Lexa, O., Štípská, P., Racek, M., Tajcmanova, L., Konopasek, J., … Lehmann, J. (2008). Vertical extrusion and horizontal channel flow of orogenic lower crust: key exhumation mechanisms in large hot orogens? *Journal of Metamorphic Geology*, 26, 273–297.

Schulz, B., & von Raumer, J.F. (1993). Syndeformational Uplift of Variscan High-pressure Rocks (Col de Bérard, Aiguilles Rouges Massif, Western Alps). *Zeitschrift der Deutschen Geologischen Gesellschaft,* 144, 104-20.

Schulz, B., & von Raumer, J. (2011). Discovery of Ordovician–Silurian metamorphic monazite in garnet metapelites of the Alpine External Aiguilles Rouges Massif. *Swiss Journal of Geosciences*, 104, 67–79. doi:10.1007/s00015-010-0048-7.

Simonetti, M., Carosi, R., Montomoli, C., Cottle, J. M., & Law, R. D. (2020a). Transpressive Deformation in the Southern European Variscan Belt: New Insights From the Aiguilles Rouges Massif (Western Alps). Tectonics, 39. https://doi.org/10.1029/2020TC006153

Simonetti, M., Carosi, R., Montomoli, C., Corsini, M., Petroccia, A., Cottle, J. M., & Iaccarino, S. (2020b). Timing and kinematics of flow in a transpressive dextral shear zone, Maures Massif (Southern France). *International Journal of Earth Sciences*, 109, 2261–2285. https://doi.org/10.1007/s00531-020-01898-6

Soula, J.C., Debat, P., Brusset, S., Bessiere, G., Christophoul, F., Deramond, J. 2001. Thrust-related, diapiric, and extensional doming in a frontal orogenic wedge: example of the Montagne Noire, southern French Hercynian Belt. *Journal of Structural Geology*, 23,1677–1699.

Spalla, M.I., Lardeaux, J.M., Dal Piaz, G.V., Gosso, G., & Messiga, B. (1996). Tectonic significance of Alpine eclogites. *Journal of Geodynamics,* 21 (3), 257–285

Stampfli, G. M., Hochard, C., Vérard, C., Wilhem, C., & von Raumer, J. (2013). The formation of Pangea. *Tectonophysics,* 593, 1-19.

Stampfli, G. M., von Raumer, J. F., & Borel, G. D. (2002). Paleozoic evolution of pre-Variscan terranes:From Gondwana to the Variscan collision. *Geological Society of America Special Paper,* 364: 263-280.

Stacey, J.S., & Kramers, J.D. (1975). Approximation of terrestrial lead isotope evolution by a two-stage model. *Earth Planetary Science Letters*, 26, 207–226.

Steiger, R.H., & Jäger, E. (1977). Subcommission on geochronology: convention on the use of decay constants in geo- and cosmochronology. *Earth Planetary Science Letters*, 36, 359–362.

Stern, R.A. (1997). The GSC sensitive high resolution ion micro-probe (SHRIMP): analytical techniques of zircon U–Th–Pb age determinations and performance evaluation. Radiogenic Age and Isotopic Studies. *Geological Survey of Canada, Current Research*, 10, 1–31.

Štípská, P., & Powell, R. (2005). Constraining the P–T path of a MORB-type eclogite using pseudosections, garnet zoning and garnet–clinopyroxene thermometry: an example from the Bohemian Massif. *Journal of Metamorphic Geology*, 23, 725–743.

Štípská, P., Pitra, P., & Powell, R. (2006). Separate or shared metamorphic histories of eclogites and surrounding rocks? An example from the Bohemian Massif. *Journal of Metamorphic Geology,* 24, 219–240.

Sun, S.S., & McDonough, W.F. (1989). Chemical and isotopic systematics of oceanic basalts: implications for mantle composition and processes. In: Saunders AD, Norry MJ (eds) Magmatism in the Ocean Basins, vol 42. *Geological Society of London*, *Special Publication*, 313–345.

Sun, J.F., Yang, J.H., Wu, F.Y., Xie, L.W., Yang, Y.H., Liu, Z.C., Li, X.H. (2012). In situ U–Pb dating of titanite by LA–ICPMS. *Chinese Science Bulletin*, 57(20), 2506–2516.

Tedeschi, M., Lanari, P., Rubatto, D., Pedrosa-Soares, A., Hermann, J., Dussin, I., … Baumgartner, L. (2017). Reconstruction of multiple P-T-t stages from retrogressed mafic rocks: Subduction versus collision in the Southern Brasília orogen (SE Brazil). *Lithos*, 294-295, 283-303. http://doi.org/10.1016/j.lithos.2017.09.025.

Teipel, U., Eichhorn, R., Loth, G., Rohrmüller, J., Höll, R., & Kennedy, A. (2004). U–Pb SHRIMP and Nd isotopic data from the western Bohemian Massif (Bayerischer Wald, Germany): implications for Upper Vendian and Lower Ordovician magmatism. *International Journal of Earth Sciences*, 93, 782–801.

Trap, P., Faure, M., Lin, W., Augier, R., Fouassier, A. (2011). Syn-collisional channel flow and exhumation of Paleoproterozoic High Pressure rocks in the Trans-North China Orogen: the critical role of partial-melting and orogenic bending. *Gondwana Research*, 20, 498–515.

Trap, P., Roger, F., Cenki-Tok, B., & Paquette, J.L. (2017). Timing and duration of partial melting and magmatism in the Variscan Montagne Noire gneiss done (French Massif Central). *International Journal of Earth Sciences*, 106, 453–476. doi:10.1007/s00531-016-1417-x

Tomkins, H.S., Powell, R., & Ellis, D.J. (2007). The pressure dependence of the zirconium-in-rutile thermometer. *Journal of Metamorphic Geology*, 25, 703–713.

van Achterbergh, E., Ryan, C.G., Jackson, S.E., & Griffin, W.L., (2001). Data reduction software for LA-ICP-MS. In Laser ablation-ICPMS in the earth science. P. Sylvester ed. *Mineralogical Association of Canada*, 29, 239-243.

van Keken, P.E., Hacker, B.R., Syracuse, E.M., Abers, G. (2011). Subduction factory: 4. Depth-dependent flux of H2O from subducting slabs worldwide. *Journal of Geophysical Research* 116, B01401.

Vanderhaeghe, O. (2009). Migmatites, granites and orogeny: flow modes of partially-molten rocks and magmas associated with melt/solid segregation in orogenic belts. *Tectonophysics*, 477, 119–134.

Vanderhaeghe, O., Laurent, O., Gardien, V., Moyen, J.F., Gébelin, A., Chelle-Michou, C., … Bellanger, M. (2020). Flow of partially molten crust controlling construction, growth and collapse of the Variscan orogenic belt: the geologic record of the French Massif Central. *Bulletin de la Société géologique de France*, 191, doi.org/10.1051/bsgf/2020013.

Vermeesch, P. (2012). On the visualisation of detrital age distributions. *Chemical Geology*, 312-313, 190-194.

von Raumer, J.F., & Bussy, F. (2004). Mont-Blanc and Aiguilles-Rouges: Geology of their polymetamorphic basement (External massifs, France-Switzerland): *Mémoires de Géologie (Lausanne)*, 42, 1–203.

von Raumer, J.F., Galetti, G., Oberhansli, R., & Pfeifer, H.R. (1990). Amphibolites from Lac Emosson/Aiguilles Rouges, Switzerland: tholeiitic basalts at a transition zone between continental and oceanic crust. *Schweizerische Mineralogische und Petrographische Mitteilungen*, 703, 419–435.

von Raumer, J. F., Stampfli, G. M., Arenas, R., & Sánchez Martínez, S. (2015). Ediacaran to Cambrian oceanic rocks of the Gondwana margin and their tectonic interpretation. *International Journal of Earth Sciences*, 104, 1107-1121. https://doi.org/10.1007/s00531-015-1142-x

Waters, D. (2003). P-T path from Cpx-Hbl-Pl symplectites, updated 22 February 2003: http://www.earth.ox.ac.uk/~davewa/research/eclogites/symplectites.html (July 2012).

Wiedenbeck, M., Allé, P., Corfu, F., Griffin, W.L., Meier, M., Oberli, F., … Spiegel, W. (1995) Three natural zircon standards for U-Th-Pb, Lu-Hf, trace element and REE analyses. *Geostandards Newsletter*, 19(1), 1-23.

White, R.W., Powell, R., Holland, T.J.B. & Worley, B.A. (2000). The effect of TiO2 and Fe2O3 on metapelitic assemblages at greenschist and amphibolite facies conditions: mineral equilibria calculations in the system K2O-FeO-MgO-Al2O3-SiO2-H2O-TiO2-Fe2O3. *Journal of Metamorphic Geology*, 18, 497–511.

White, R.W., Powell, R., Holland, T.J.B., Johnson, T.E. & Green, E.C.R. (2014). New mineral activity–composition relations for thermodynamic calculations in metapelitic systems. *Journal of Metamorphic Geology*, 32, 261–286.

Whitney, D. L., Roger, F., Teyssier, C., Rey, P.F., & Respaut, J.P. (2015). Syn-collapse eclogite metamorphism and exhumation of deep crust in a migmatite dome: The P–T–t record of the youngest Variscan eclogite (Montagne Noire, French Massif Central). *Earth Planetary Science Letters*, 430, 224-234.

Whitney, D. L., Hamelin, C., Teyssier, C., Raia, N. H., Korchinski, M. S., Seaton, N. C. A., ... & Rey, P. F. (2020). Deep crustal source of gneiss dome revealed by eclogite in migmatite (Montagne Noire, French Massif Central). *Journal of Metamorphic Geology*, 38, 297–327.

Zhang, G.B., Ellis, D., Christy, A., Zhang, L.F., & Song, S.G. (2010). Zr-in-rutile thermometry in HP/UHP eclogites from Western China. *Contributions to Mineralogy and Petrology*, 160, 427–439.

Fig 1

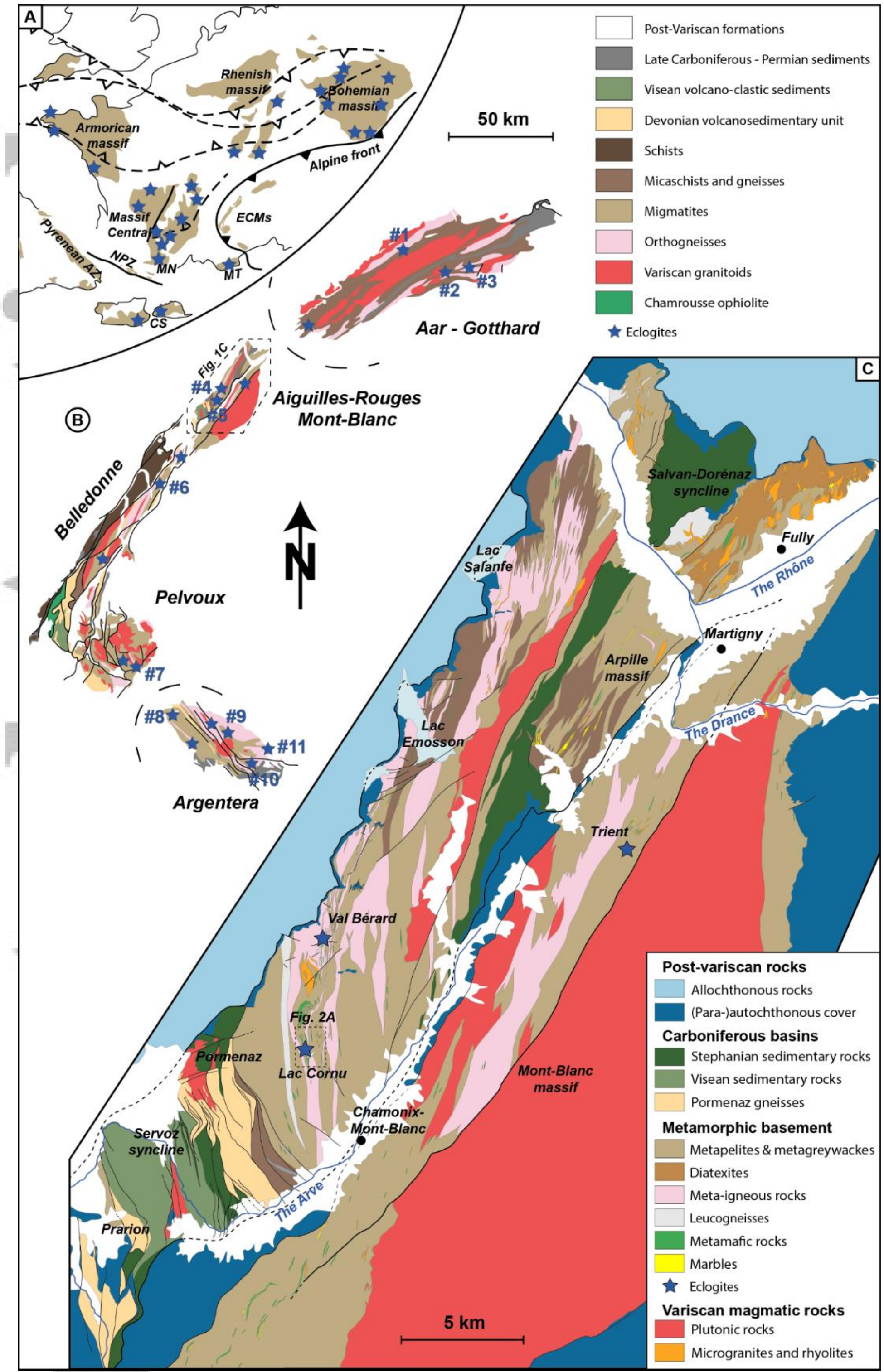
A
Rhenish massif
Bohemian massif
Armorican massif
Alpine front
Massif Central
ECMs
Pyrenean AZ
NPZ
MN
MT
CS
50 km
#1
#2
#3
Aar - Gotthard
Fig. 1C
#4
#5
Aiguilles-Rouges Mont-Blanc
B
Belledonne
#6
Pelvoux
N
#7
#8
#9
#11
#10
Argentera
Post-Variscan formations
Late Carboniferous - Permian sediments
Visean volcano-clastic sediments
Devonian volcanosedimentary unit
Schists
Micaschists and gneisses
Migmatites
Orthogneisses
Variscan granitoids
Chamrousse ophiolite
Eclogites
C
Salvan-Dorénaz syncline
Fully
The Rhône
Lac Salanfe
Martigny
Arpille massif
Lac Emosson
The Drance
Trient
Val Bérard
Fig. 2A
Lac Cornu
Pormenaz
Mont-Blanc massif
Chamonix-Mont-Blanc
Servoz syncline
The Arve
Prarion
5 km
Post-variscan rocks
Allochthonous rocks
(Para-)autochthonous cover
Carboniferous basins
Stephanian sedimentary rocks
Visean sedimentary rocks
Pormenaz gneisses
Metamorphic basement
Metapelites & metagreywackes
Diatexites
Meta-igneous rocks
Leucogneisses
Metamafic rocks
Marbles
Eclogites
Variscan magmatic rocks
Plutonic rocks
Microgranites and rhyolites

Fig. 2

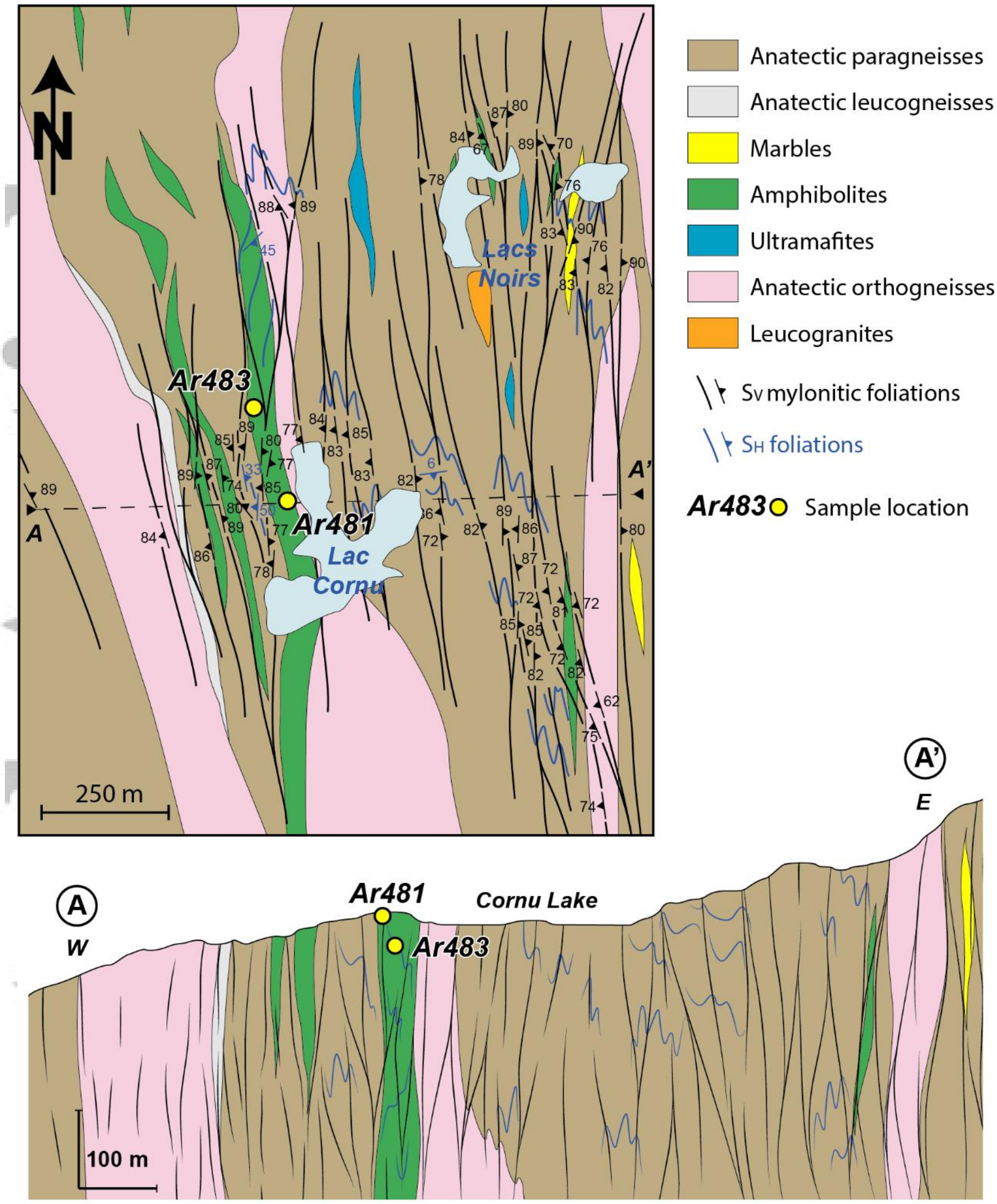

Anatectic paragneisses
Anatectic leucogneisses
Marbles
Amphibolites
Ultramafites
Anatectic orthogneisses
Leucogranites
Sv mylonitic foliations
SH foliations
Ar483 Sample location
Ar483
Ar481
Lacs Noirs
Lac Cornu
250 m
A
A'
W
E
Cornu Lake
100 m

Fig. 3

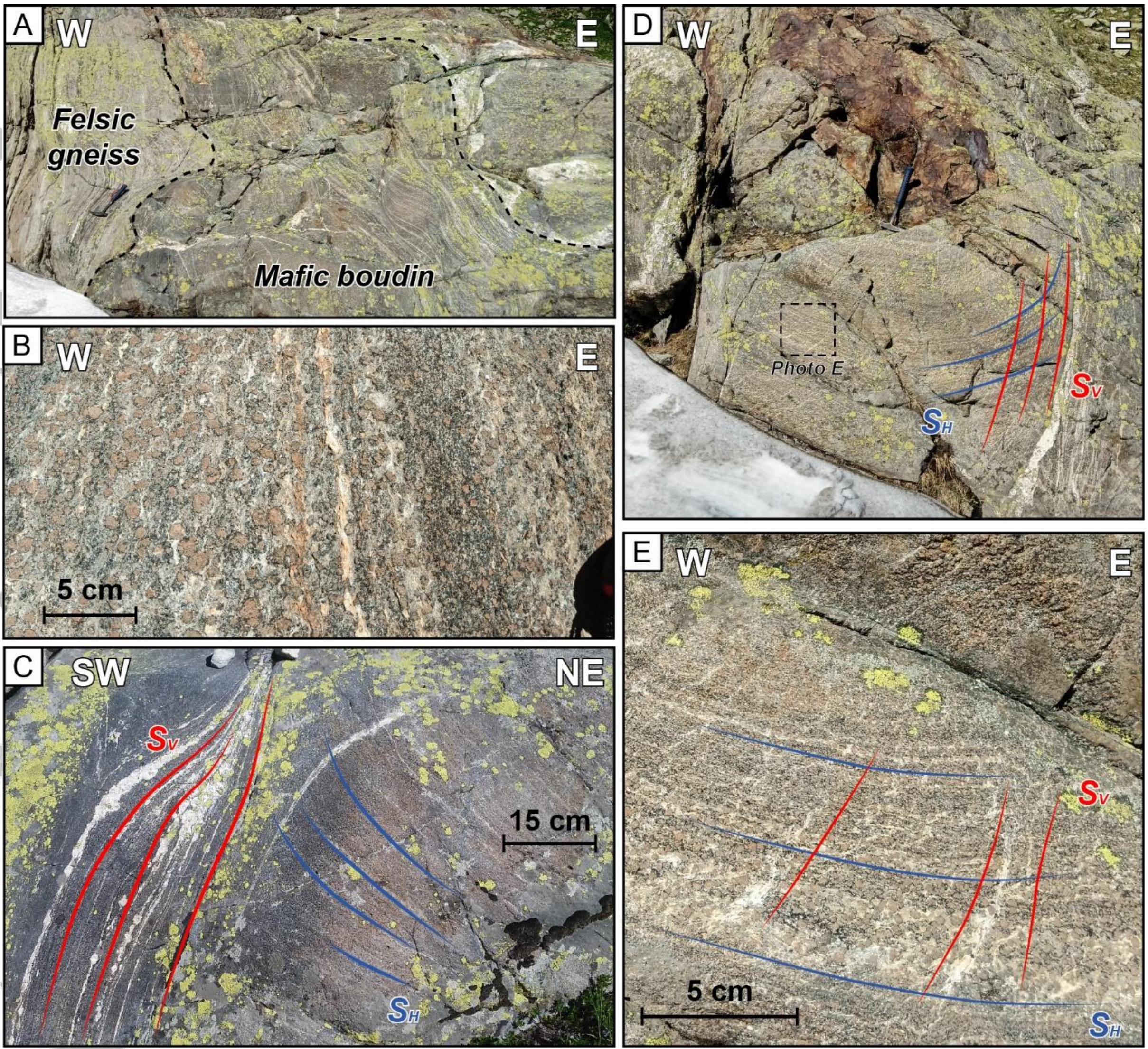

A
W
E
Felsic gneiss
Mafic boudin
B
W
E
5 cm
C
SW
NE
S_V
15 cm
S_H
D
W
E
Photo E
S_V
S_H
E
W
E
S_V
5 cm
S_H

Fig. 4

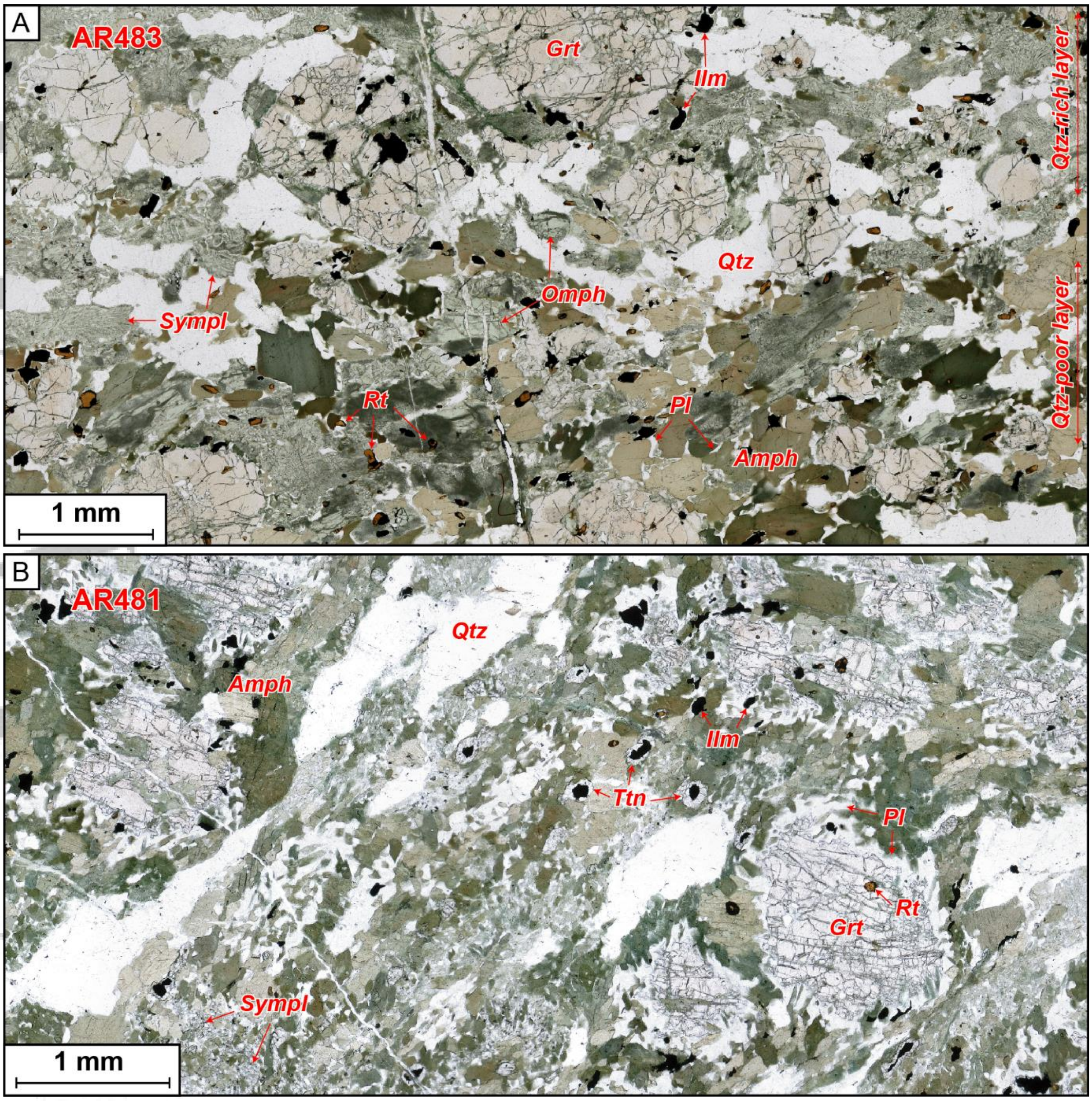
A
AR483
Grt
Ilm
Qtz
Omph
Sympl
Rt
Pl
Amph
Qtz-rich layer
Qtz-poor layer
1 mm
B
AR481
Qtz
Amph
Ilm
Ttn
Pl
Rt
Grt
Sympl
1 mm

Fig. 5

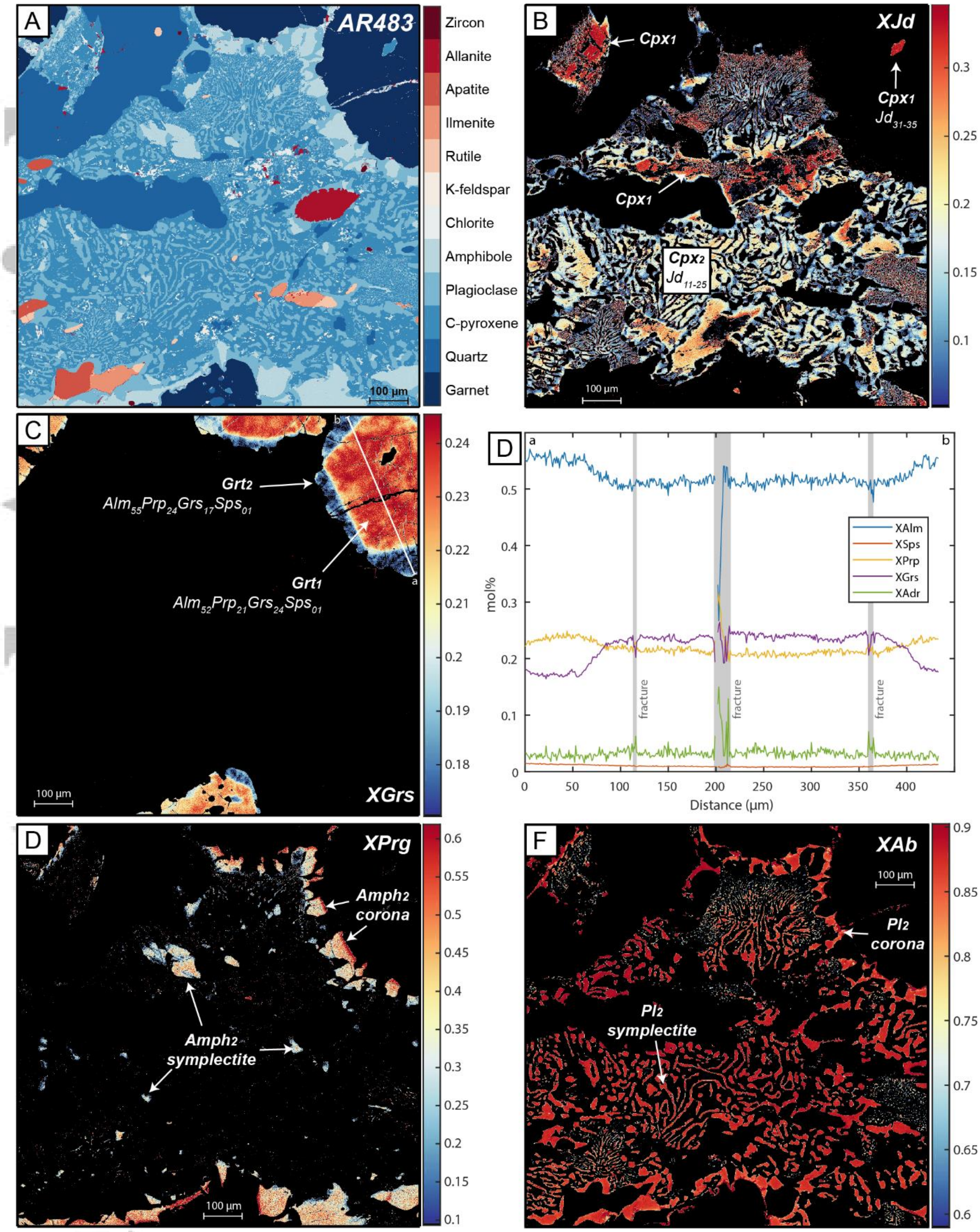

A
AR483
100 µm
Zircon
Allanite
Apatite
Ilmenite
Rutile
K-feldspar
Chlorite
Amphibole
Plagioclase
C-pyroxene
Quartz
Garnet
B
XJd
Cpx1
Cpx1
Jd31-35
Cpx1
Cpx2
Jd11-25
100 µm
0.3
0.25
0.2
0.15
0.1
C
Grt2
Alm55Prp24Grs17Sps01
Grt1
Alm52Prp21Grs24Sps01
100 µm
XGrs
0.24
0.23
0.22
0.21
0.2
0.19
0.18
D
XAlm
XSps
XPrp
XGrs
XAdr
mol%
fracture
fracture
fracture
Distance (µm)
D
XPrg
Amph2
corona
Amph2
symplectite
100 µm
0.6
0.55
0.5
0.45
0.4
0.35
0.3
0.25
0.2
0.15
0.1
F
XAb
100 µm
Pl2
corona
Pl2
symplectite
0.9
0.85
0.8
0.75
0.7
0.65
0.6

Fig. 6

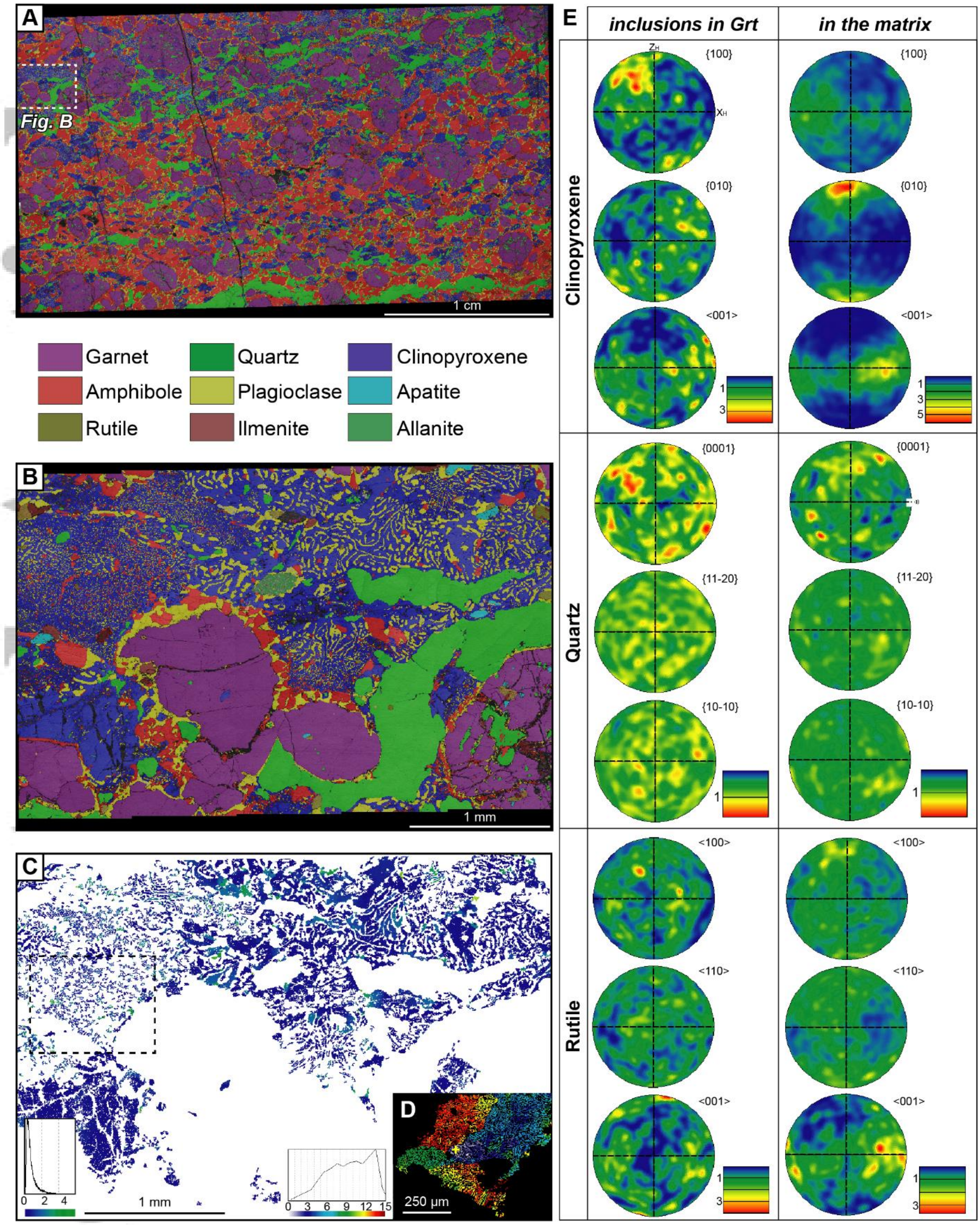

A
Fig. B
1 cm
Garnet
Quartz
Clinopyroxene
Amphibole
Plagioclase
Apatite
Rutile
Ilmenite
Allanite
B
1 mm
C
1 mm
D
250 µm
E
inclusions in Grt
in the matrix
Clinopyroxene
{100}
{010}
<001>
Quartz
{0001}
{11-20}
{10-10}
Rutile
<100>
<110>
<001>

Fig. 7

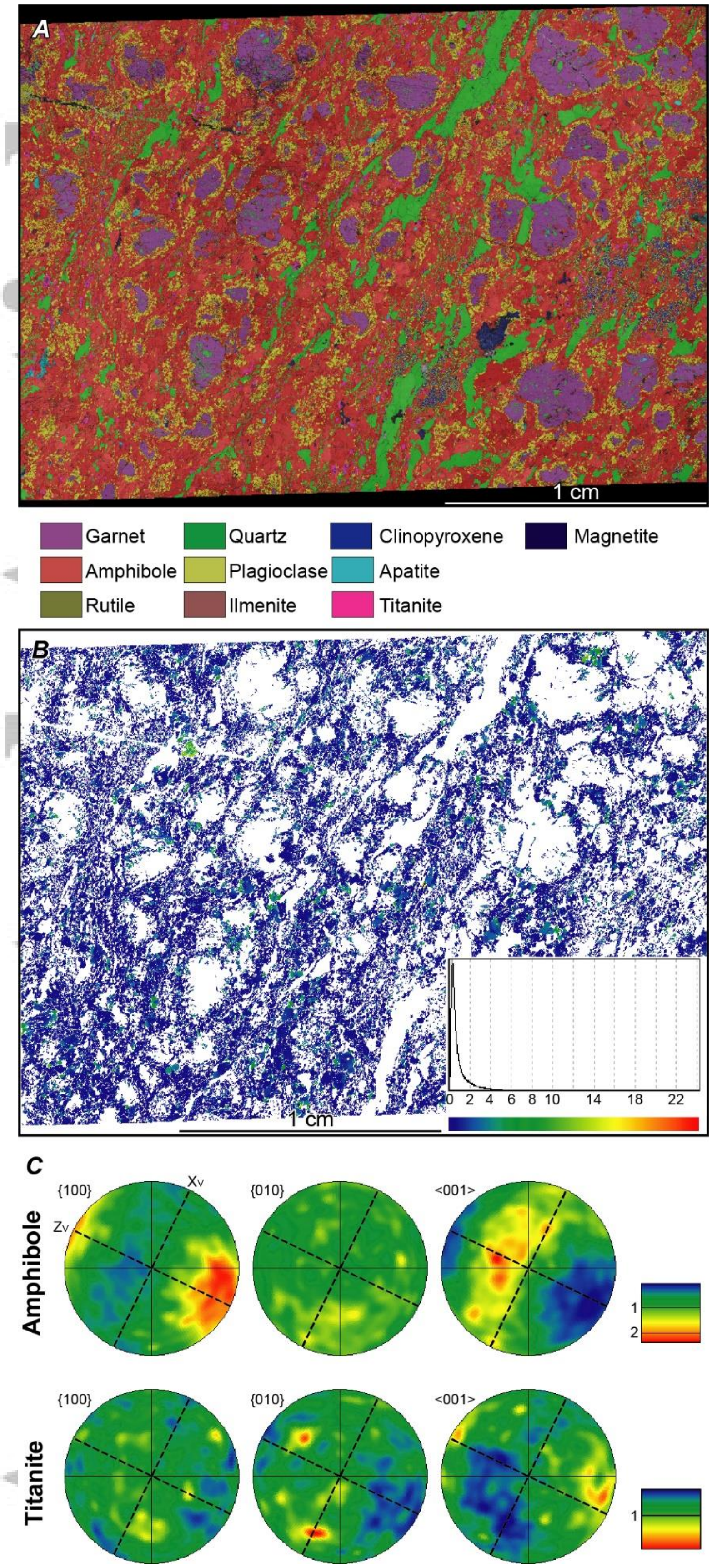
A
1 cm
Garnet
Quartz
Clinopyroxene
Magnetite
Amphibole
Plagioclase
Apatite
Rutile
Ilmenite
Titanite
B
1 cm
0 2 4 6 8 10 14 18 22
C
Amphibole
{100}
{010}
<001>
Xv
Zv
1
2
Titanite
{100}
{010}
<001>
1

Fig. 9

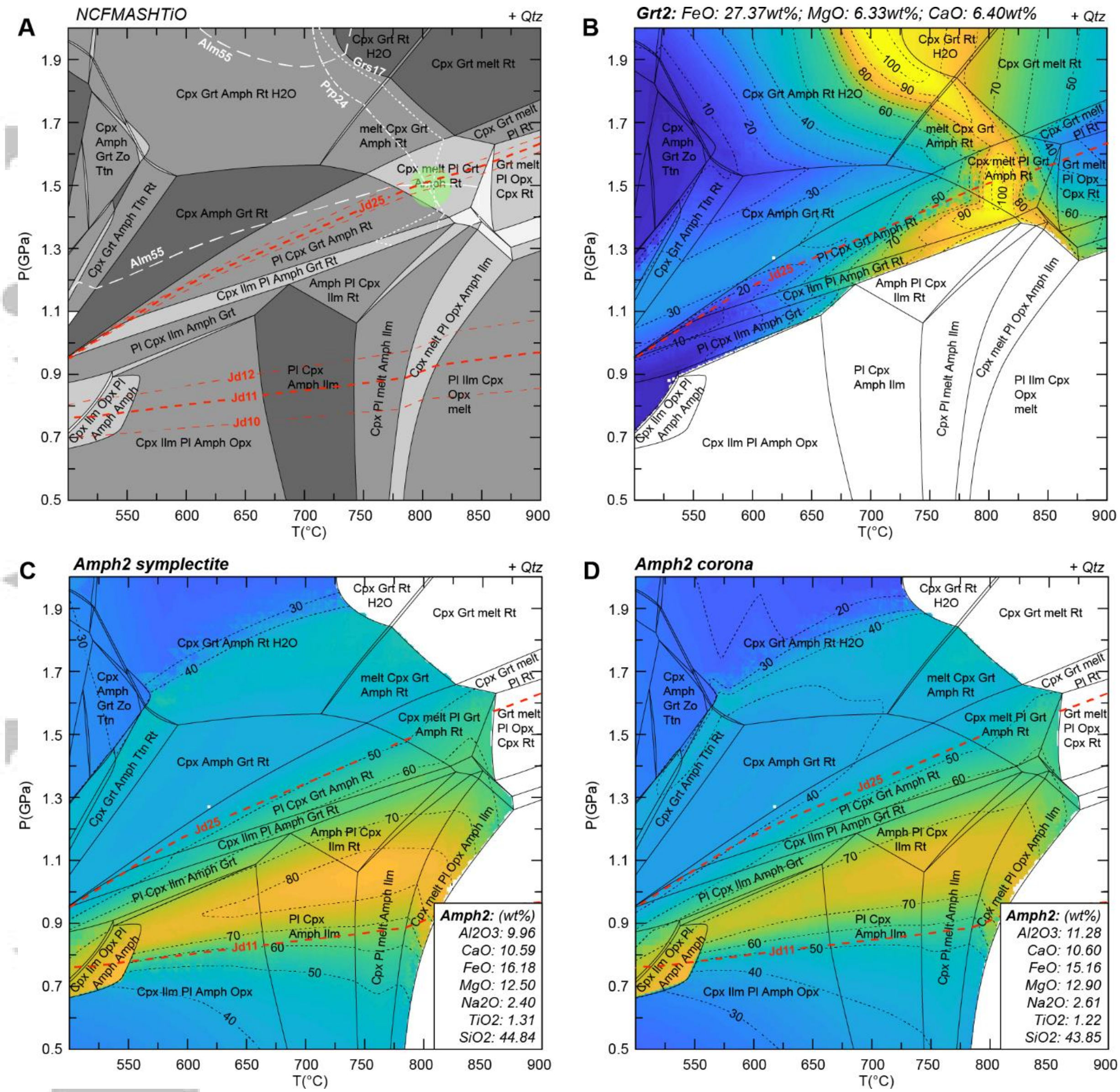
A
NCFMASHTiO
+ Qtz
B
Grt2: FeO: 27.37wt%; MgO: 6.33wt%; CaO: 6.40wt%
C
Amph2 symplectite
D
Amph2 corona
Cpx Grt Amph Rt H2O
Cpx Grt melt Rt
Cpx Grt Rt H2O
melt Cpx Grt Amph Rt
Cpx melt Pl Grt Amph Rt
Grt melt Pl Opx Cpx Rt
Cpx Amph Grt Zo Ttn
Cpx Grt Amph Ttn Rt
Cpx Amph Grt Rt
Pl Cpx Grt Amph Rt
Cpx Ilm Pl Amph Grt Rt
Amph Pl Cpx Ilm Rt
Pl Cpx Ilm Amph Grt
Pl Cpx Amph Ilm
Cpx Pl melt Amph Ilm
Cpx melt Pl Opx Amph Ilm
Pl Ilm Cpx Opx melt
Cpx Ilm Opx Pl Amph Amph
Cpx Ilm Pl Amph Opx
Alm55
Grs17
Prp24
Jd25
Jd12
Jd11
Jd10
P(GPa)
T(°C)
Amph2: (wt%)
Al2O3: 9.96
CaO: 10.59
FeO: 16.18
MgO: 12.50
Na2O: 2.40
TiO2: 1.31
SiO2: 44.84
Amph2: (wt%)
Al2O3: 11.28
CaO: 10.60
FeO: 15.16
MgO: 12.90
Na2O: 2.61
TiO2: 1.22
SiO2: 43.85

Fig. 10

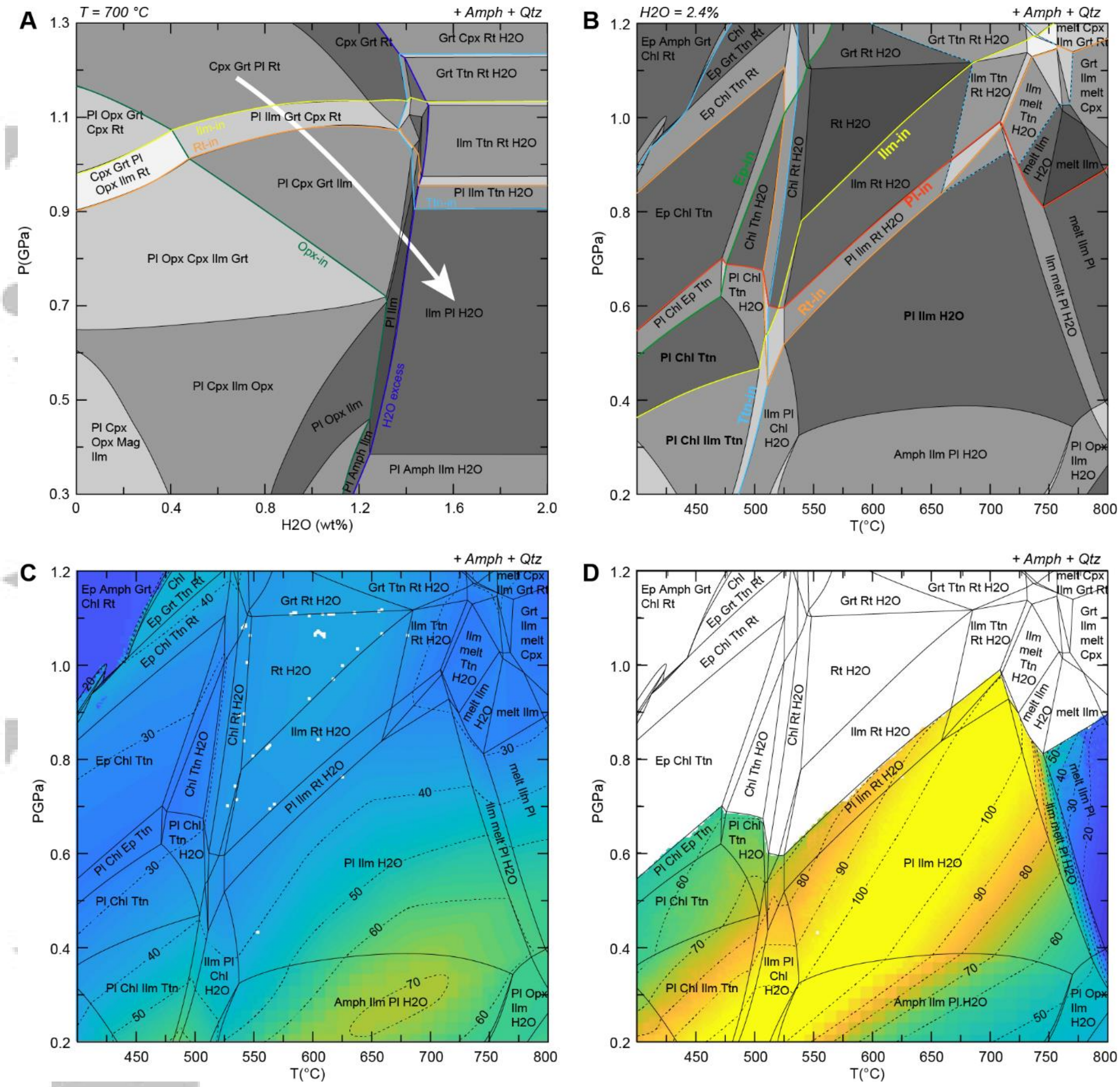
A
T = 700 °C
+ Amph + Qtz
P(GPa)
H2O (wt%)
Cpx Grt Pl Rt
Cpx Grt Rt
Grt Cpx Rt H2O
Grt Ttn Rt H2O
Pl Opx Grt Cpx Rt
Pl Ilm Grt Cpx Rt
Ilm Ttn Rt H2O
Cpx Grt Pl Opx Ilm Rt
Pl Cpx Grt Ilm
Pl Ilm Ttn H2O
Pl Opx Cpx Ilm Grt
Opx-in
Ilm Pl H2O
Pl Cpx Ilm Opx
Pl Opx Ilm
H2O excess
Pl Cpx Opx Mag Ilm
Pl Amph Ilm H2O
B
H2O = 2.4%
+ Amph + Qtz
PGPa)
T(°C)
Ep Amph Grt Chl Rt
Grt Rt H2O
Grt Ttn Rt H2O
Ilm Ttn Rt H2O
Rt H2O
Ilm-in
Ilm Rt H2O
Pl-in
Ep Chl Ttn
Pl Ilm Rt H2O
Rt-in
Pl Ilm H2O
Pl Chl Ttn
Pl Chl Ilm Ttn
Amph Ilm Pl H2O
melt Ilm
Ilm melt Pl H2O
C
+ Amph + Qtz
PGPa)
T(°C)
D
+ Amph + Qtz
PGPa)
T(°C)

Fig. 11

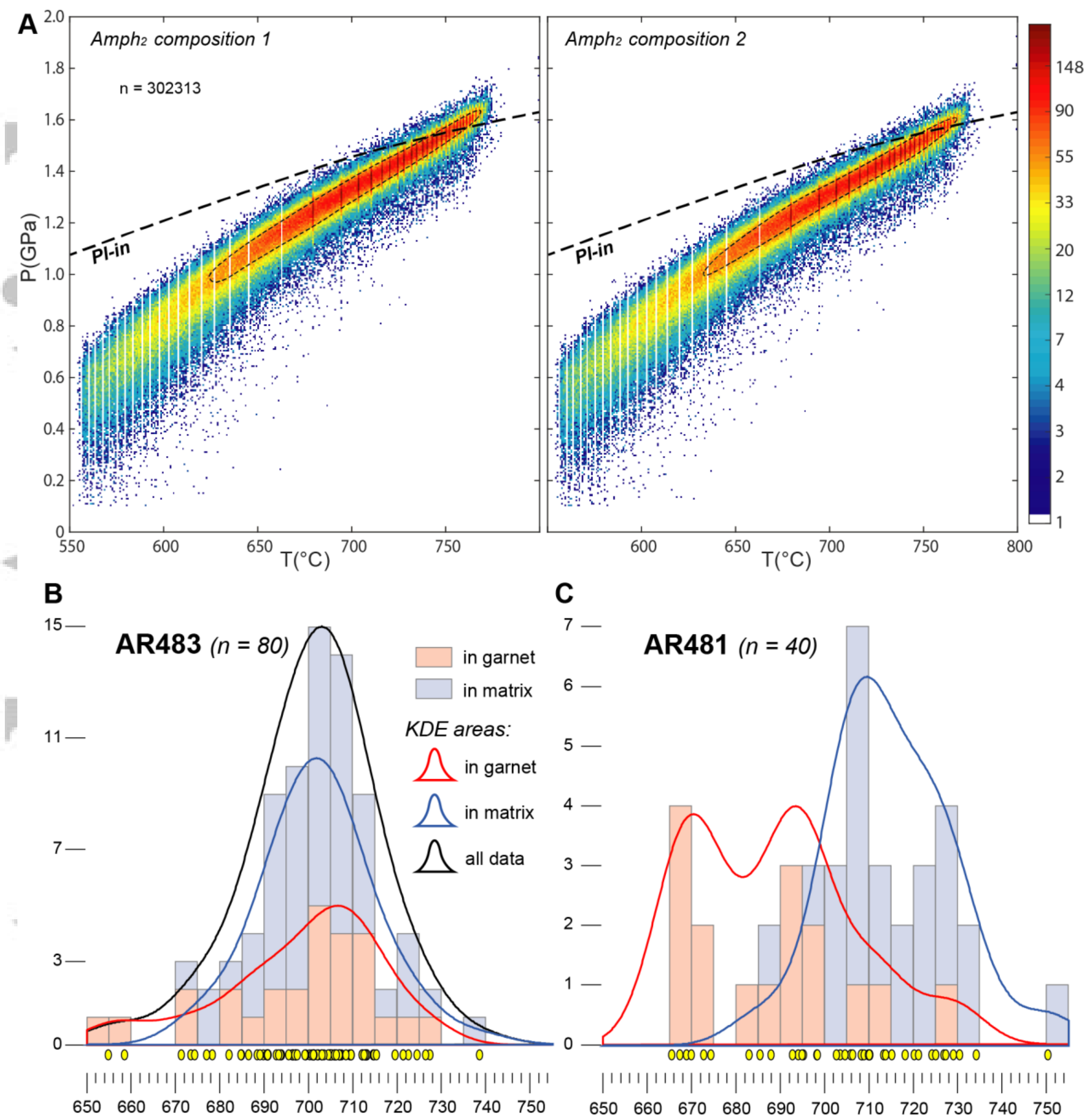
A
Amph2 composition 1
n = 302313
Pl-in
P(GPa)
T(°C)
Amph2 composition 2
Pl-in
T(°C)
B
AR483 (n = 80)
in garnet
in matrix
KDE areas:
in garnet
in matrix
all data
C
AR481 (n = 40)

Fig. 12

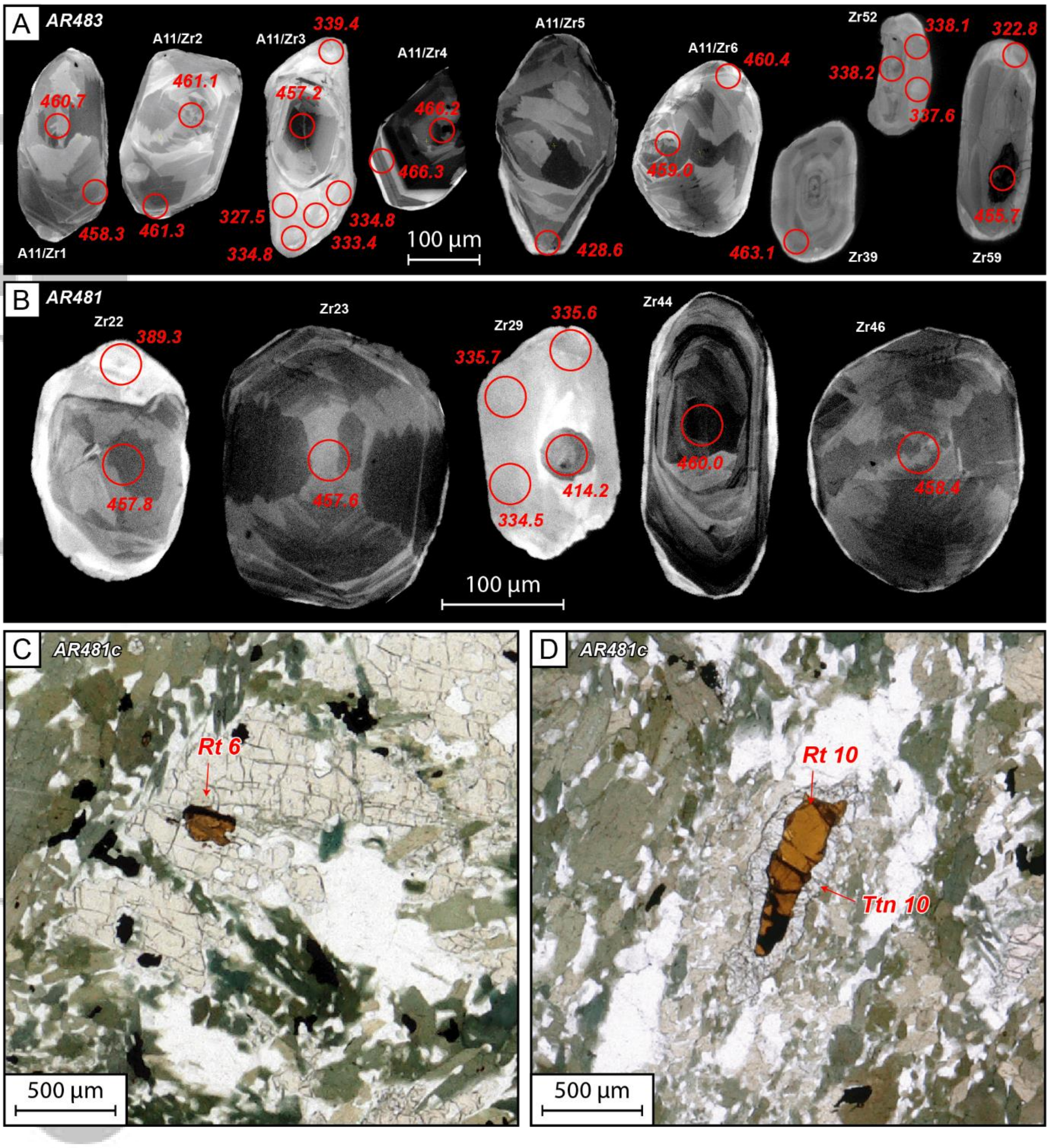
A AR483
A11/Zr1
A11/Zr2
A11/Zr3
A11/Zr4
A11/Zr5
A11/Zr6
Zr52
Zr39
Zr59
460.7
458.3
461.1
461.3
339.4
457.2
327.5
334.8
333.4
334.8
466.2
466.3
428.6
460.4
459.0
463.1
338.1
338.2
337.6
322.8
455.7
100 µm
B AR481
Zr22
Zr23
Zr29
Zr44
Zr46
389.3
457.8
457.6
335.6
335.7
414.2
334.5
460.0
458.4
100 µm
C AR481c
Rt 6
500 µm
D AR481c
Rt 10
Ttn 10
500 µm

Fig. 13

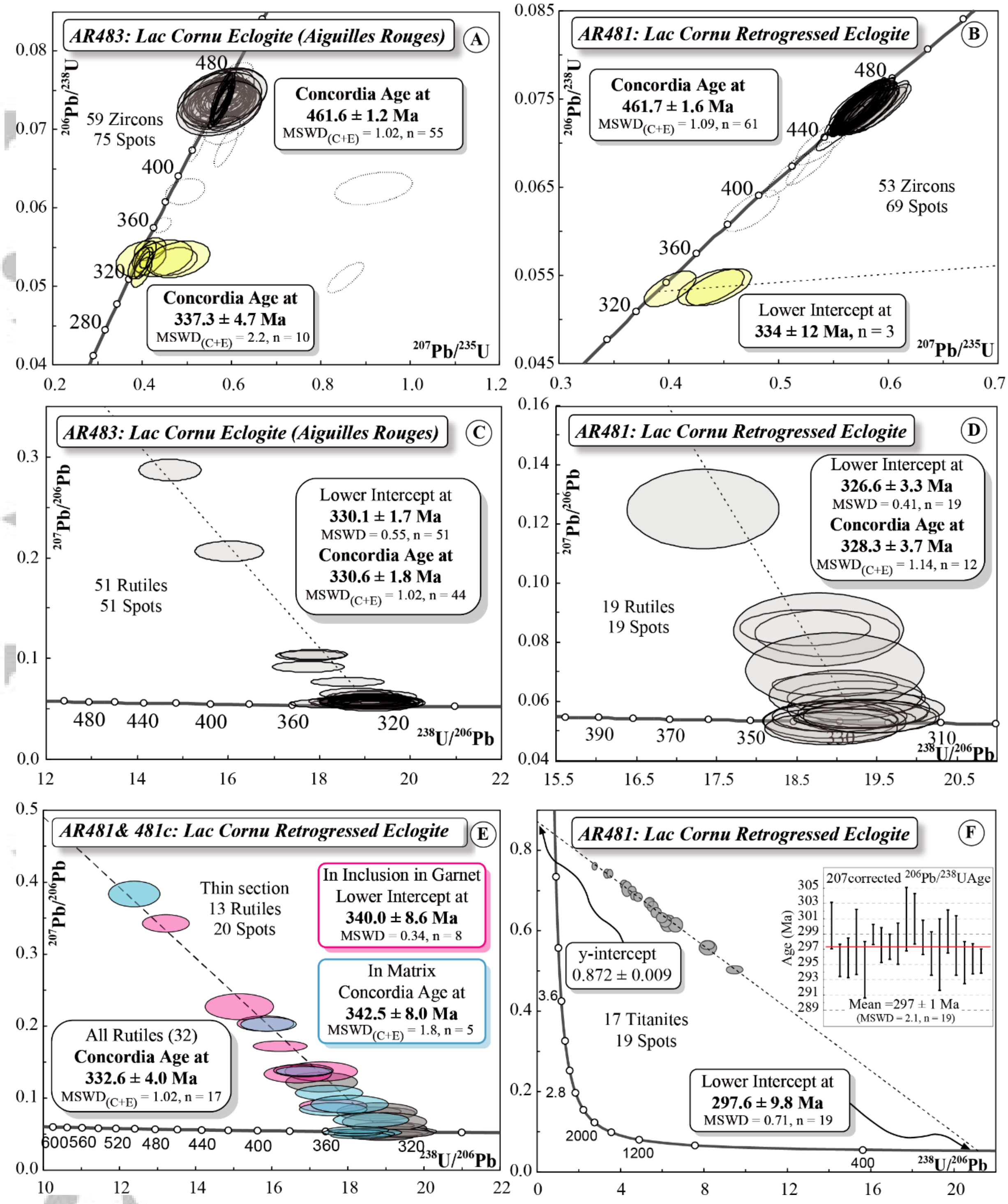

AR483: Lac Cornu Eclogite (Aiguilles Rouges)
A
59 Zircons
75 Spots
Concordia Age at
461.6 ± 1.2 Ma
MSWD(C+E) = 1.02, n = 55
Concordia Age at
337.3 ± 4.7 Ma
MSWD(C+E) = 2.2, n = 10
AR481: Lac Cornu Retrogressed Eclogite
B
Concordia Age at
461.7 ± 1.6 Ma
MSWD(C+E) = 1.09, n = 61
53 Zircons
69 Spots
Lower Intercept at
334 ± 12 Ma, n = 3
AR483: Lac Cornu Eclogite (Aiguilles Rouges)
C
51 Rutiles
51 Spots
Lower Intercept at
330.1 ± 1.7 Ma
MSWD = 0.55, n = 51
Concordia Age at
330.6 ± 1.8 Ma
MSWD(C+E) = 1.02, n = 44
AR481: Lac Cornu Retrogressed Eclogite
D
19 Rutiles
19 Spots
Lower Intercept at
326.6 ± 3.3 Ma
MSWD = 0.41, n = 19
Concordia Age at
328.3 ± 3.7 Ma
MSWD(C+E) = 1.14, n = 12
AR481& 481c: Lac Cornu Retrogressed Eclogite
E
Thin section
13 Rutiles
20 Spots
In Inclusion in Garnet
Lower Intercept at
340.0 ± 8.6 Ma
MSWD = 0.34, n = 8
In Matrix
Concordia Age at
342.5 ± 8.0 Ma
MSWD(C+E) = 1.8, n = 5
All Rutiles (32)
Concordia Age at
332.6 ± 4.0 Ma
MSWD(C+E) = 1.02, n = 17
AR481: Lac Cornu Retrogressed Eclogite
F
y-intercept
0.872 ± 0.009
17 Titanites
19 Spots
207corrected 206Pb/238UAge
Age (Ma)
Mean =297 ± 1 Ma
(MSWD = 2.1, n = 19)
Lower Intercept at
297.6 ± 9.8 Ma
MSWD = 0.71, n = 19

Fig. 14

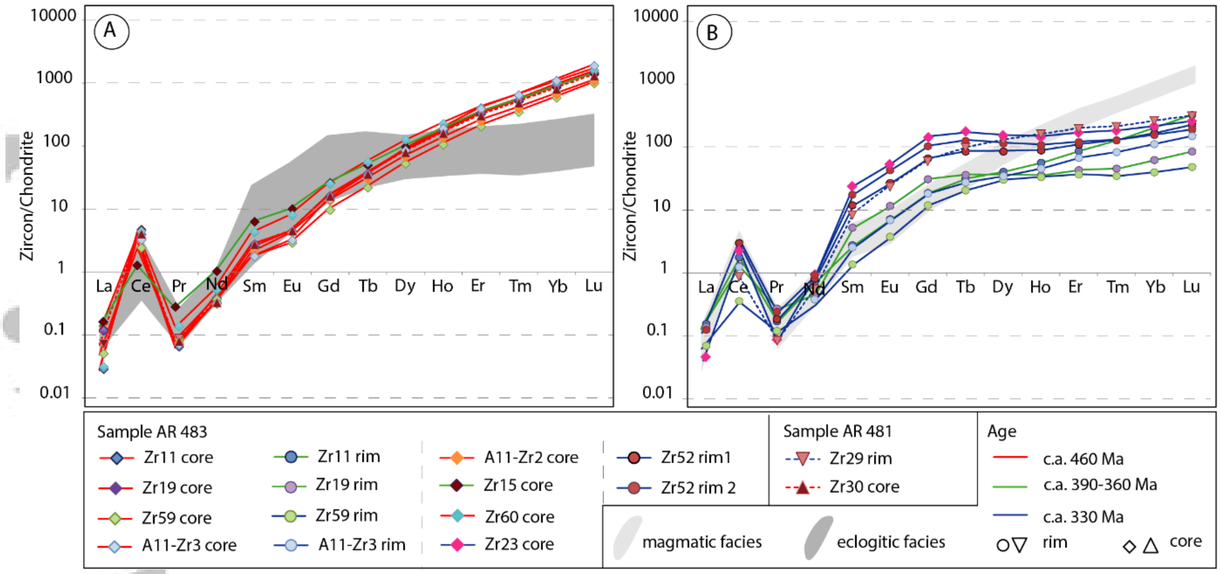

A
B
10000
1000
100
10
1
0.1
0.01
Zircon/Chondrite
La
Ce
Pr
Nd
Sm
Eu
Gd
Tb
Dy
Ho
Er
Tm
Yb
Lu
Sample AR 483
Zr11 core
Zr19 core
Zr59 core
A11-Zr3 core
Zr11 rim
Zr19 rim
Zr59 rim
A11-Zr3 rim
A11-Zr2 core
Zr15 core
Zr60 core
Zr23 core
Zr52 rim1
Zr52 rim 2
Sample AR 481
Zr29 rim
Zr30 core
Age
c.a. 460 Ma
c.a. 390-360 Ma
c.a. 330 Ma
rim
core
magmatic facies
eclogitic facies

Fig. 15

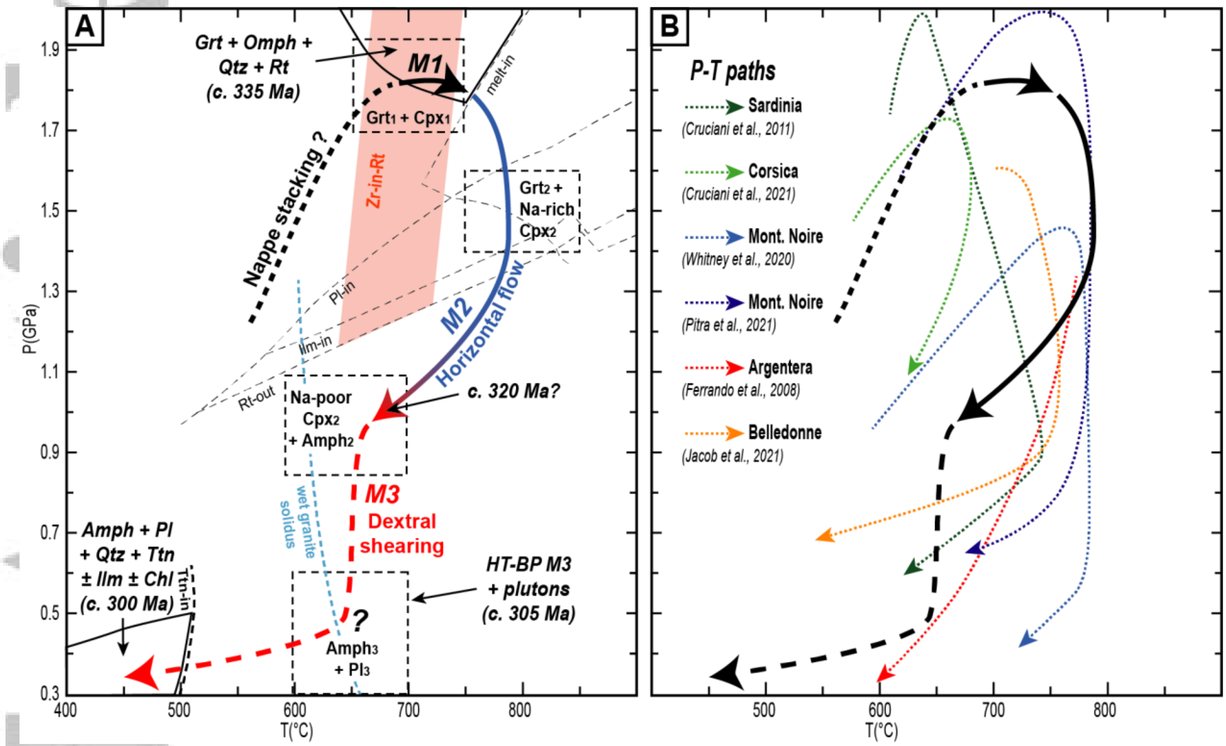

A
B
Grt + Omph +
Qtz + Rt
(c. 335 Ma)
M1
Grt1 + Cpx1
melt-in
Nappe stacking ?
Zr-in-Rt
Grt2 +
Na-rich
Cpx2
Pl-in
Ilm-in
Rt-out
M2
Horizontal flow
c. 320 Ma?
Na-poor
Cpx2
+ Amph2
M3
Dextral
shearing
wet granite
solidus
Amph + Pl
+ Qtz + Ttn
± Ilm ± Chl
(c. 300 Ma)
Ttn-in
HT-BP M3
+ plutons
(c. 305 Ma)
?
Amph3
+ Pl3
P(GPa)
T(°C)
P-T paths
Sardinia
(Cruciani et al., 2011)
Corsica
(Cruciani et al., 2021)
Mont. Noire
(Whitney et al., 2020)
Mont. Noire
(Pitra et al., 2021)
Argentera
(Ferrando et al., 2008)
Belledonne
(Jacob et al., 2021)

Table 1. Eclogitic metabasites characteristics in the ECMs. The ages are ± 2□. ID-TIMS: Isotopic Dilution Thermal Ionization; LA-ICPMS: Laser Ablation-Inductively Coupled Mass Spectrometry EMPA: Electron Probe MicroAnalysis; SHRIMP: Sensitive High Resolution Ion Microprobe; LI: Lower Intercept; Zr: zircon; Mz: monazite; Rt: rutile; Amph: amphibole. Previous works: (a) Schaltegger et al., 2003; (b) Abrecht & Biino, 1994; (c) Oberli et al., 1994; (d) Mercolli et al., 1994; (e) Abrecht et al., 1991; (f) Biino, 1994; (g) Gebauert et al. 1988; (h) Schulz & von Raumer, 1993; (i) Schulz & von Raumer, 2011; (j) Paquette et al., 1989; (k) Liégeois & Duchesne, 1981; (l) Bussy et al., 2011; (m) Jacob et al., 2021; (n) Fréville et al, 2016; (o) Latouche & Bogdanoff, 1987; (p) Rubatto et al., 2001; (q) Jouffray et al., 2020; (r) Ferrando et al., 2008 and (s) Rubatto et al., 2010.

Massif (refences)	n°	Locality	Protolith geochemistry	Protolith age (± 2σ)	Method	HP conditions	HP metamorphism age (± 2σ)	Method
Aar (a)	1	Sustenhorn	Gabbros	478 ± 5 Ma	ID-TIMS (Zr)			
Gothard (b - g)	2	Kastelhorn	Gabbros with island arc affinity	467-475 Ma	ID-TIMS (Zr)			
	3	Val Naps	N-MORB tholeiite and gabbros with island arc affinity	467-475 Ma or c. 870 Ma	ID-TIMS (Zr)	700-750°C 1.8 GPa	468-461 Ma	ID-TIMS (Zr)
	4	Val Bérard				700 ± 50°C 1.4 ± 0.1 GPa		

Aiguilles-Rouges (h -l)	5	Lac Cornu	N-MORB tholeiite in thin continental crust	453 +3/-2 Ma 463 +3/-2 Ma 458 ± 5 Ma	ID-TIMS (Zr) LA-ICPMS (Zr) LA-ICPMS (Zr)	c. 780°C ≥1.1 GPa	345 ± 14 Ma	LA-ICPMS (Zr)
Belledonne (j-m)	6	Lac des Tempètes	N-MORB tholeiite in thin continental crust	456 ± 4 Ma 448 ± 6 Ma	LA-ICPMS (Zr) LA-ICPMS (Zr)	690-740°C ≥1.4 GPa	~ 395 Ma 340 ± 11 Ma	ID-TIMS (Zr) – LI LA-ICPMS (Rt)
Pelvoux (n)	7	Peyre-Arguet		471 ± 5 Ma	LA-ICPMS (Zr)			
Argentera (o - s ; j)	8	Rabuons				c. 660-800°C 1.4 GPa		
	9	Val Meris	Basalt	457 ± 6 Ma 462 + 6 Ma	SHRIMP (Zr) ID-TIMS (Zr)			
	10	Madone de Fenestre	N-MORB, E-MORB and cumulates with crustal contamination	471 +40/-29 Ma	ID-TIMS (Zr)	640–740 °C 1.5 ± 0.25 GPa	~ 424 Ma > 339.7 ± 12 Ma	ID-TIMS (Zr) – LI $^{40}Ar/^{39}Ar$ (Amph)
	11	Frisson lakes		486 ± 7 Ma	SHRIMP (Zr)	735 ± 15°C 1.38 ± 0.05 GPa	340.7 ± 4.2 336.3 ± 4.1 Ma	SHRIMP (Zr)